Research Square

Preprints are preliminary reports that have not undergone peer review. They should not be considered conclusive, used to inform clinical practice, or referenced by the media as validated information.

Modeling Capillary Heterogeneity in Geological CO2 Storage via Finite-volume Discretization with Interface Conditions

Ammar Alali

ammara@stanford.edu

Stanford University

Bradley Mallison

Omar Duran

Stanford University

Hamdi Tchelepi

Stanford University

Research Article

Keywords: CCS, Two-phase flow and transport, Capillarity-dominated flow, Implicit finite-volume schemes, Interface conditions

Posted Date: October 22nd, 2026

DOI: https://doi.org/10.21203/rs.3.rs-11354970/v1

License: This work is licensed under a Creative Commons Attribution 4.0 International License. Read Full License

Additional Declarations: No competing interests reported.

Modeling Capillary Heterogeneity in Geological CO_2 Storage via Finite-volume Discretization with Interface Conditions

Ammar H. Alali[a,*], Bradley T. Mallison, Omar Duran[a], Hamdi A. Tchelepi[a]

[a] *Energy Science and Engineering Department, Stanford University, USA*

Abstract

Capillary heterogeneity plays an important role in determining CO_2 plume migration paths and the amount of CO_2 that can be stored in geological formations, yet standard numerical simulation schemes require excessive grid refinement to accurately resolve capillary-driven trapping at material interfaces. In this work, we present a finite-volume scheme for immiscible two-phase flow that incorporates discrete interface conditions to enforce local capillary equilibrium at rock-type boundaries. The enhanced scheme, referred to as PPU-C, is based on the standard Phase-Potential Upwinding (PPU) method and utilizes a local nonlinear solver at each material interface to enforce capillary pressure continuity and flux conservation. We extend prior formulations by improving the efficiency of the local solver, incorporating capillary pressure and relative permeability hysteresis, and implementing the scheme within the open-source GEOS simulation framework for direct application to geological carbon storage problems. The method is compared to PPU through four numerical examples of increasing complexity: a 1D gravity segregation case, its 3D extension both in drainage-only and hysteretic settings, and a 2D domain with multiple barriers. Finally, we conclude with a field-scale 2D cross-section based on the SPE-11B benchmark. Results show that PPU-C significantly improves the accuracy of predicted capillary and residual trapping volumes on practical grids with a modest computational overhead that does not exceed 25% in our tests. These findings demonstrate that the use of interface conditions is a practical and efficient numerical technique to accurately model capillary heterogeneity in large-scale CO_2 storage simulations.

Keywords: CCS, Two-phase flow and transport, Capillarity-dominated flow, Implicit finite-volume schemes, Interface conditions.

1. Introduction

Geological carbon storage (GCS) in saline aquifers and depleted hydrocarbon reservoirs has been recognized as an important enabler in the global effort to address climate change (IPCC, 2022). It involves injecting supercritical CO_2 deep underground, where it can remain permanently trapped, preventing its release into the atmosphere (Orr Jr, 2004; Metz et al., 2005; Townsend et al., 2020). Among the different GCS options, saline aquifers are the most widely used (Bruant et al., 2002; Pruess et al., 2003).

For CO_2 storage in saline aquifers, four main subsurface mechanisms contribute to the trapping of CO_2, as outlined by Flett et al. (2004) and Benson et al. (2005). Mineral trapping occurs due to the reaction of rock minerals with injected CO_2, and is considered an important mechanism in the long term (Bachu et al., 1994). Dissolution trapping is caused by the solubility of CO_2 in the formation brine (Ennis-King and Paterson, 2002), and the subsequent increase in brine density that leads to convective mixing and gravity fingering phenomena (Riaz et al., 2006). Structural and stratigraphic trapping refers to the accumulation of large CO_2 volumes beneath a cap rock, similar to the formation of hydrocarbon reservoirs (Gluyas and Swarbrick, 2021). While capillarity impacts the integrity of cap rock seals, capillary trapping within saline aquifers is a separate and critical mechanism for CO_2 storage (Krevor et al., 2015). This mechanism can be further categorized into residual trapping, which arises from pore-scale flow mechanics due to disconnection of CO_2 into immobile and mobile fractions in a multiphase flow environment, and

*Corresponding author

capillary heterogeneity trapping, sometimes referred to as capillary pinning. Residual trapping, driven by snap-off, is influenced by hysteresis effects in the capillary pressure and relative permeability functions (Lenormand et al., 1983) and plays a major role in the overall CO_2 sequestration process (Flett et al., 2004; Spiteri and Juanes, 2006). Capillary heterogeneity trapping is due to local and abrupt changes in rock properties (Saadatpoor et al., 2010), primarily due to entry pressure jumps between rock types. Recent reviews by Zhang et al. (2025) and Ni et al. (2025) highlight the criticality of capillary heterogeneity trapping for GCS and the challenge of accurately capturing its influence in large-scale simulations. High-resolution simulation models are required to resolve the key physical mechanisms (Kovscek et al., 2024; Kachuma et al., 2026).

The development of efficient multiphase modeling and simulation frameworks has leveraged experience of simulation for hydrocarbon production (Aziz and Settari, 1979) and been tailored to the mechanisms and scales for GCS (Nordbotten and Celia, 2011). Resolving heterogeneous capillarity in GCS simulations remains a significant challenge for current methods. In heterogeneous models, the relative permeability and capillary pressure are spatially discontinuous between different rock types, leading to complex capillary-driven flow dynamics. These discontinuities arise because capillary pressure depends not only on saturation but also on intrinsic rock properties exhibiting large and abrupt spatial variations, such as the pore throat size and wettability. Therefore, it is essential to design an accurate and specialized numerical scheme and solution strategy able to capture abrupt spatial jumps in the relative permeability and capillary pressure functions.

To address this challenge, we will adopt the concept of interface conditions, as proposed Van Duijn et al. (1995), which have been used in the finite-volume method to improve the accuracy of the flux in the presence of capillary heterogeneity (Enchéry et al., 2006; Cancès, 2009; Evje and Friis, 2012; Brenner et al., 2013; Hamon et al., 2018; Ahmed et al., 2018; Bassetto et al., 2022). Interface conditions have initially been applied to ensure physically consistent simulations of capillary trapping taking place during drainage in the context of DNAPL trapping (Niessner et al., 2005), and more recently, to represent capillary imbibition in matrix-fracture systems (Brenner et al., 2017, 2018; Aghili et al., 2019; Alali et al., 2021; Brenner et al., 2022). Moreover, they have been combined with a hysteresis model within a vertex-based finite volume method (Papafotiou et al., 2010) and successfully demonstrated a more accurate representation of flow dynamics, even on coarser grids. However, the use of discrete interface conditions is not yet common in practical GCS simulations. Notably, among the fully implicit finite-volume simulators that participated in the SPE-11 benchmark study, none reported the use of numerical schemes enhanced with interface conditions (Nordbotten et al., 2025), which further motivates the present work.

This work improves prior formulations (Hamon et al., 2018; Alali et al., 2021) that used saturations as the primary variable in the interface problem and required variable switching to handle changes between single-phase and two-phase flow states. Here, we present a simpler local solver that avoids variable switching by using an interface capillary pressure as the primary variable. Hysteresis is included to allow modeling of residual trapping combined with capillary heterogeneity trapping. We implement the improved method in the open-source GEOS simulation framework (Settgast et al., 2024) for large-scale GCS applications and coupled subsurface processes (Bui et al., 2021; Chehade et al., 2024). Our focus here is on immiscible flows but the GEOS implementation also supports compositional simulations. Results for GCS simulations with discrete interface conditions and dissolution trapping will be shared in a forthcoming publication. In our numerical examples, we investigate the accuracy improvement and computational efficiency, including multidimensional settings and the field-scale SPE-11B benchmark (Nordbotten et al., 2024), compared to standard flux approximations to highlight that compute cost is not an obstacle to practical adoption of interface conditions. In fact, our results show that the overhead of enforcing interface conditions remains modest and below 25% in all cases. In a few cases, the enhanced scheme achieved better efficiency than the standard approach because it required fewer nonlinear iterations.

2. Mathematical model

2.1. Governing equations

In this section, we describe the mathematical formulation to model immiscible isothermal and compressible flow in subsurface porous media. We consider a two-component system of gas and water flow in

a compressible porous medium, in which each component exists only in its corresponding phase: vapor or liquid brine. The gas and water components are denoted by the subscripts g and w, respectively. The liquid, which is the wetting phase, and the vapor, the non-wetting phase, are denoted by the subscripts ℓ and v, respectively. The mass conservation law reads

$$\frac{\partial}{\partial t}\left(\phi \rho_p S_p\right) + \nabla \cdot \left(\rho_p \boldsymbol{u}_p\right) = \rho_p q_p, \quad \text{for} \quad p \in \{\ell, v\}, \tag{1}$$

where $\phi(\mathbf{x})$ is the porosity of the medium, which can vary spatially and is a function of the phase pressure, denoted as $p_p(\mathbf{x}, t)$, $S_p(\mathbf{x}, t)$ is the phase saturation, and t is the time. The source/sink term q_p is positive for injection and negative for production. The phase density, ρ_p, is a function of the pressure, whereas the phase velocity, $\boldsymbol{u}_p$, is defined using the multiphase extension of Darcy's law as

$$\boldsymbol{u}_p := -k\lambda_p(\nabla p_p - \rho_p g \nabla z), \quad \text{for} \quad p \in \{\ell, v\}, \tag{2}$$

Here, $k(\mathbf{x})$ is the scalar absolute permeability of the medium, λ_p is the phase mobility defined as k_{rp}/μ_p, where $k_{rp}(\mathbf{x}, S_p)$ is the phase relative permeability, and μ_p is the phase viscosity which is a function of the pressure. In both phases, we assume that the relative permeability is a strictly increasing function of the phase saturation. We denote gravitational acceleration by g and depth by z. The conservation of mass equations are constrained by a volume balance of $S_\ell + S_v = 1$ and a capillary pressure constraint that relates the two phase pressures with $P_c(S_\ell) = p_v - p_\ell$.

2.2. Rock types

In heterogeneous porous media, the saturation functions, namely capillary pressure and relative permeability, are discontinuous across material interfaces, due to changes in intrinsic properties such as the pore throat size distribution and wettability (Leverett, 1941). To account for this rock type heterogeneity, we divided the domain (Ω) into a finite number of non-overlapping subdomains Ω_α such that $\cup_\alpha \Omega_\alpha = \Omega$. In this study, we use phase relative permeability and capillary pressure functions that are distinct for each rock type. In particular, the numerical examples that will be presented are based on the SPE11 benchmark case that consists of 7 rock types (Nordbotten et al., 2024).

We rely on Brooks and Corey (1964) capillary pressure model defined as

$$P_c^{(\alpha)}(S_\ell) := p_e^{(\alpha)} \overline{S_\ell}^{(-1/\theta^{(\alpha)})}, \tag{3}$$

where $p_e^{(\alpha)}$ is the entry pressure which can be defined based on the J-Leverett equation as a function of rock porosity and permeability, and $\theta^{(\alpha)}$ determines the saturation exponent. Both parameters are distinct for each rock type. The liquid effective saturation is defined as:

$$\overline{S_\ell} = \frac{S_\ell - S_{\ell,c}^{(\alpha)}}{1 - S_{\ell,c}^{(\alpha)} - S_{v,r}^{(\alpha)}} \tag{4}$$

where $S_{\ell,c}^{(\alpha)}$ is the minimum (connate) wetting phase saturation, and $S_{v,r}^{(\alpha)}$ is the minimum (residual) non-wetting phase saturation. Also, the non-wetting phase effective saturation can be computed as $\overline{S_v} = 1 - \overline{S_\ell}$. We highlight that the capillary pressure curve obtained with the Brooks-Corey model is unbounded when $\overline{S_\ell}$ approaches zero. Therefore, in order to avoid numerical problems with this analytical capillary pressure, a pre-processing step is adopted in the model description of SPE11 Comparative Solution Study (Nordbotten et al., 2024) by modifying the formulation given by (5) so that the capillary pressure becomes:

$$P_c^{(\alpha)}(S_\ell) := p_{\mathrm{c,max}}^{(\alpha)} \mathrm{erf}\left(\frac{p_e^{(\alpha)} \overline{S_\ell}^{(-1/\theta^{(\alpha)})}}{p_{\mathrm{c,max}}^{(\alpha)}} \frac{\sqrt{\pi}}{2}\right), \tag{5}$$

This procedure smoothly enforces an upper bound on capillary pressure while preserving its monotonicity and differentiability. The relative permeabilities are defined using Corey (1954) as:

$$k_{rp}^{(\alpha)}(S_p) = \overline{S_p}^{\Lambda_p^{(\alpha)}} \tag{6}$$

where $\Lambda_p^{(\alpha)}$ is the saturation exponent. The saturation exponents ($\Lambda_p^{(\alpha)}$) and ($\theta_p^{(\alpha)}$) must satisfy Burdine's definition (Burdine, 1953) of relative permeability based on the integral of capillary pressure, which ensures that the resulting diffusion coefficient degenerates at endpoints. Figure 1 shows the saturation functions used in this work for two rock types from SPE11.

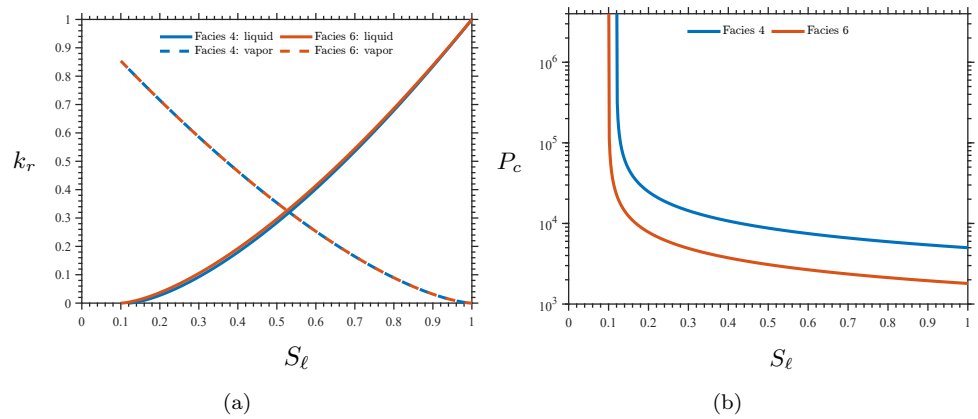

Figure 1: *Relative permeability in (a) and capillary pressures (Pa) in (b) for two rock regions from SPE11.*

We assume these saturation functions are monotone, with the caveat that capillary pressure must be a strictly decreasing function of the wetting-phase saturation.

2.3. Hysteresis

The saturation functions are not only discontinuous across material interfaces but also depend on saturation history. To model hysteretic saturation functions, multiple numerical models were developed, including Killough (1976), Carlson (1981), and Larsen and Skauge (1998). In this work, we rely on Killough's model for both the wetting and non-wetting phases. This model generates scanning curves between bounding drainage and imbibition curves based on the flow-reversal history. The following formulation applies to any arbitrary sequence of drainage and imbibition cycles.

Throughout this section, we write every constitutive function with its arguments stated explicitly: current liquid saturation S_ℓ (or vapor saturation $S_v = 1 - S_\ell$) is the primary independent variable, and any history variables appear after a semicolon, e.g., $P_c^{(\alpha)}(S_\ell; S_\ell^g, S_{v,h})$. The hysteresis mode at a particular location can be described by three history variables: (i) the maximum historical vapor saturation $S_{v,h} = \max_{\tau \le t} S_v(\tau)$; (ii) the reversal saturation S_ℓ^Δ, recorded for the most recent flow switch from drainage to imbibition or vice versa; and (iii) the ghost departure saturation, S_ℓ^g, which is a virtual saturation that anchors the active capillary pressure scanning curve and is recomputed at every flow reversal. The active hysteresis mode is selected by the sign of $\partial S_\ell/\partial t$, which indicates whether the system is undergoing drainage ($\partial S_\ell/\partial t < 0$) or imbibition ($\partial S_\ell/\partial t > 0$).

2.3.1. Bounding curves

Both the drainage and imbibition bounding curves are based on the same Brooks–Corey capillary pressure (5) and Corey relative permeability (6) definitions introduced in Section 2.2; they are functions of the current saturation only, parameterized by the rock type. The main distinction between the two bounding processes is the residual vapor saturation: primary drainage starts from a fully liquid-saturated state and leaves no residual vapor, whereas imbibition traps a maximum residual vapor saturation $S_{v,r}^{\max,(\alpha)}$ on the bounding curve. Accordingly, the effective liquid saturations of the two processes are functions of S_ℓ alone,

$$\overline{S}_\ell^{dr}(S_\ell) = \frac{S_\ell - S_{\ell,c}^{(\alpha)}}{1 - S_{\ell,c}^{(\alpha)}}, \qquad \overline{S}_\ell^{im}(S_\ell) = \frac{S_\ell - S_{\ell,c}^{(\alpha)}}{1 - S_{\ell,c}^{(\alpha)} - S_{v,r}^{\max,(\alpha)}}, \tag{7}$$

where $S_{\ell,c}^{(\alpha)}$ is the connate liquid saturation, and the effective vapor saturations are defined as $\overline{S}_v = 1 - \overline{S_\ell}$ for both processes. The bounding drainage and imbibition capillary pressures are then

$$P_{c,dr}^{(\alpha)}(S_\ell) = p_e^{(\alpha)} \left(\overline{S}_\ell^{\,dr}(S_\ell)\right)^{(-1/\theta_{dr}^{(\alpha)})}, \qquad P_{c,im}^{(\alpha)}(S_\ell) = p_e^{(\alpha)} \left[\left(\overline{S}_\ell^{\,im}(S_\ell)\right)^{(-1/\theta_{im}^{(\alpha)})} - 1\right], \tag{8}$$

and the bounding drainage and imbibition relative permeabilities are

$$k_{rp,dr}^{(\alpha)}(S_p) = \left(\overline{S}_p^{\,dr}(S_p)\right)^{\Lambda_{p,dr}^{(\alpha)}}, \qquad k_{rp,im}^{(\alpha)}(S_p) = \left(\overline{S}_p^{\,im}(S_p)\right)^{\Lambda_{p,im}^{(\alpha)}}. \tag{9}$$

In this work, we utilize the drainage capillary pressure and relative permeability curves defined in Section 2.2 for the bounding curves, and we generate consistent imbibition counterparts that share the same exponents, $\theta_{im}^{(\alpha)} = \theta_{dr}^{(\alpha)}$ and $\Lambda_{p,im}^{(\alpha)} = \Lambda_{p,dr}^{(\alpha)}$, entry pressures, and differ solely through the residual trapping $S_{v,r}^{\max,(\alpha)}$ and hence the imbibition effective saturation $\overline{S}_p^{\,im}$, as shown in Figure 2.

For each rock type, the residual trapping is determined using the Land model (Land, 1968) as a function of the Land trapping coefficient given, for the vapor phase, by

$$C_v^{(\alpha)} = \frac{1}{S_{v,r}^{\max,(\alpha)}} - \frac{1}{S_{v,\max}^{(\alpha)}}, \tag{10}$$

where $S_{v,\max}^{(\alpha)} = 1 - S_{\ell,c}^{(\alpha)}$ is the maximum attainable vapor saturation, and $C_v^{(\alpha)}$ is constant for each rock type. The trapping coefficient for the liquid phase is calculated analogously using the respective bounding-curve endpoints. Since the bounding curves used in this work utilize an imbibition maximum liquid saturation that coincides with the vapor curves, $S_{v,r}^{\max,(\alpha)}$, this results in $C_\ell^{(\alpha)} = C_v^{(\alpha)}$.

2.3.2. Scanning curves

A critical aspect of the history dependence of the saturation functions enters through the residually-trapped saturation for each scanning curve. Following the Land model, the residual vapor saturation reached by imbibition from the maximum historical vapor saturation $S_{v,h}$ is

$$S_{v,r}^{(\alpha)}(S_{v,h}) = \frac{S_{v,h}}{1 + C_v^{(\alpha)} S_{v,h}}, \tag{11}$$

and, due to the choice of the bounding curves in this work, this value is used to obtain the maximum liquid saturation reached by imbibition as $S_{\ell,\max}^{(\alpha)}(S_{v,h}) = 1 - S_{v,r}^{(\alpha)}(S_{v,h})$. The Land trapping vapor saturation enters the capillary pressure and vapor relative permeability scanning curves, and the counterpart Land maximum liquid saturation enters the liquid relative permeability scanning curves.

Capillary pressure hysteresis. During primary drainage or imbibition, the capillary pressure is a function of the current saturation only, $P_c^{(\alpha)} = P_{c,dr}^{(\alpha)}(S_\ell)$ or $P_{c,im}^{(\alpha)}(S_\ell)$ per (8). After a flow reversal is detected, when the sign of $\partial S_\ell/\partial t$ changes as the simulation progresses, the current saturation is captured as the new reversal saturation, denoted S_ℓ^Δ, and the capillary pressure follows a scanning curve obtained by interpolating between the bounding curves evaluated as:

$$P_c^{(\alpha)} = \begin{cases} P_{c,\mathrm{im(scan)}}^{(\alpha)}\left(S_\ell;\, S_\ell^g, S_{v,h}\right) = P_{c,dr}^{(\alpha)}(S_\ell) + F\left(S_\ell;\, S_\ell^g, S_{v,h}\right)\left[P_{c,im}^{(\alpha)}(S_\ell) - P_{c,dr}^{(\alpha)}(S_\ell)\right] & \text{if } \partial S_\ell/\partial t > 0, \\ P_{c,\mathrm{dr(scan)}}^{(\alpha)}\left(S_\ell;\, S_\ell^g\right) = P_{c,im}^{(\alpha)}(S_\ell) + F^\dagger\left(S_\ell;\, S_\ell^g\right)\left[P_{c,dr}^{(\alpha)}(S_\ell) - P_{c,im}^{(\alpha)}(S_\ell)\right] & \text{if } \partial S_\ell/\partial t \le 0, \end{cases} \tag{12}$$

where the imbibition and drainage Killough weighting functions are defined as

$$F\left(S_\ell; S_\ell^g, S_{v,h}\right) = \left[\frac{1}{S_\ell - S_\ell^g + \varepsilon} - \frac{1}{\varepsilon}\right]\left[\frac{1}{1 - S_{v,r}^{\alpha}(S_{v,h}) - S_\ell^g + \varepsilon} - \frac{1}{\varepsilon}\right]^{-1}, \tag{13}$$

and

$$F^\dagger\left(S_\ell; S_\ell^g\right) = \left[\frac{1}{S_\ell^g - S_\ell + \varepsilon} - \frac{1}{\varepsilon}\right]\left[\frac{1}{S_\ell^g - S_{\ell,c}^{(\alpha)} + \varepsilon} - \frac{1}{\varepsilon}\right]^{-1}. \tag{14}$$

Here $\varepsilon > 0$ is the Killough curvature parameter, and the ghost departure saturation, S_ℓ^g, is chosen to enforce capillary pressure continuity at every flow reversal.

Consider a flow reversal that occurs at S_ℓ^Δ, with its corresponding capillary pressure (P_c^Δ), then the ghost departure saturation S_ℓ^g is obtained by ensuring that a new scanning curve passes through the point $(S_\ell^\Delta, P_c^\Delta)$. For a flow that transitions into imbibition, this can be computed by solving the following equation:

$$F\big(S_\ell^\Delta;\, S_\ell^g, S_{v,h}\big) = \frac{P_c^\Delta - P_{c,dr}^{(\alpha)}(S_\ell^\Delta)}{P_{c,im}^{(\alpha)}(S_\ell^\Delta) - P_{c,dr}^{(\alpha)}(S_\ell^\Delta)}, \quad \text{and } S_\ell^g \le S_\ell^\Delta. \tag{15}$$

Whereas for a flow that transitions to drainage, S_ℓ^g is computed by solving the following analogous equation:

$$F^\dagger\big(S_\ell^\Delta;\, S_\ell^g\big) = \frac{P_c^\Delta - P_{c,im}^{(\alpha)}(S_\ell^\Delta)}{P_{c,dr}^{(\alpha)}(S_\ell^\Delta) - P_{c,im}^{(\alpha)}(S_\ell^\Delta)}, \quad \text{and } S_\ell^g \ge S_\ell^\Delta. \tag{16}$$

Substituting (13) or (14) yields a quadratic equation in S_ℓ^g, for which the physically meaningful root satisfying each respective inequality is retained. A reversal from a bounding drainage curve results in $F\big(S_\ell^\Delta;\, S_\ell^g, S_{v,h}\big) = 0$, hence S_ℓ^g to be equal to S_ℓ^Δ. Note that secondary drainage and subsequent modes are not experienced in the examples presented in this work.

Relative permeability hysteresis for the vapor phase. The vapor relative permeability during primary drainage depends on the current saturation only and follows the bounding drainage curve, $k_{rv}^{(\alpha)} = k_{rv,dr}^{(\alpha)}(S_v)$, per (9). During imbibition, when $S_v < S_{v,h}$, it becomes a function of the current vapor saturation S_v and of the maximum historical vapor saturation $S_{v,h}$, computed by scaling the bounding imbibition curve as

$$k_{rv,\mathrm{im(scan)}}^{(\alpha)}\big(S_v;\, S_{v,h}\big) = \frac{k_{rv,dr}^{(\alpha)}(S_{v,h})}{k_{rv,dr}^{(\alpha)}(S_{v,\max}^{(\alpha)})}\, k_{rv,im}^{(\alpha)}\big(\breve{S}_v(S_v;\, S_{v,h})\big), \tag{17}$$

where the normalized saturation $\breve{S}_v$ maps the current saturation from the scanning range $[S_{v,r}^{(\alpha)}(S_{v,h}),\, S_{v,h}]$ to the bounding imbibition range $[S_{v,r}^{\max,(\alpha)},\, S_{v,\max}^{(\alpha)}]$ as

$$\breve{S}_v\big(S_v;\, S_{v,h}\big) = S_{v,r}^{\max,(\alpha)} + \frac{S_v - S_{v,r}^{(\alpha)}(S_{v,h})}{S_{v,h} - S_{v,r}^{(\alpha)}(S_{v,h})}\big(S_{v,\max}^{(\alpha)} - S_{v,r}^{\max,(\alpha)}\big), \tag{18}$$

and $S_{v,r}^{(\alpha)}(S_{v,h})$ is the trapped vapor saturation from the Land model (11). Killough relative permeability hysteresis model assumes reversibility for secondary and subsequent drainage cycles, where it follows the scanning curve (17) retracing the most recent imbibition path until $S_v = S_{v,h}$ at which it rejoins the bounding drainage curve continuously.

Relative permeability hysteresis for the liquid phase. The liquid relative permeability can alternatively be computed using the minimum historical liquid saturation, $S_{\ell,h} = 1 - S_{v,h}$. During primary drainage, it depends on the current saturation only and follows the bounding drainage curve, $k_{r\ell}^{(\alpha)} = k_{r\ell,dr}^{(\alpha)}(S_\ell)$, per (9). During imbibition, it becomes a function of the current liquid saturation S_ℓ and of $S_{\ell,h}$, and it is computed by scaling the bounding imbibition curve as

$$k_{r\ell,\mathrm{im(scan)}}^{(\alpha)}\big(S_\ell;\, S_{\ell,h}\big) = k_{r\ell,dr}^{(\alpha)}(S_{\ell,h}) + \Big[k_{r\ell}^{*}(S_{\ell,h}) - k_{r\ell,dr}^{(\alpha)}(S_{\ell,h})\Big]\frac{k_{r\ell,im}^{(\alpha)}\big(1 - \breve{S}_v(S_v;\, S_{v,h})\big)}{k_{r\ell,im}^{(\alpha)}\big(1 - S_{v,r}^{\max,(\alpha)}\big)}. \tag{19}$$

The endpoint relative permeability $k_{r\ell}^*$ of the scanning curve is interpolated between the drainage curve and the bounding imbibition endpoint:

$$k_{r\ell}^{*}(S_{\ell,h}) = k_{r\ell,dr}^{(\alpha)}\big(S_{\ell,\max}^{(\alpha)}(S_{\ell,h})\big) + \Big[k_{r\ell,im}^{(\alpha)}\big(1 - S_{v,r}^{\max,(\alpha)}\big) - k_{r\ell,dr}^{(\alpha)}\big(1 - S_{v,r}^{\max,(\alpha)}\big)\Big]\left(\frac{1 - S_{\ell,\max}^{(\alpha)}(S_{\ell,h})}{S_{v,r}^{\max,(\alpha)}}\right). \tag{20}$$

The scanning curve departs continuously from the bounding drainage curve at $S_\ell = S_{\ell,h}$. As for the vapor phase, the liquid scanning curves are also reversible.

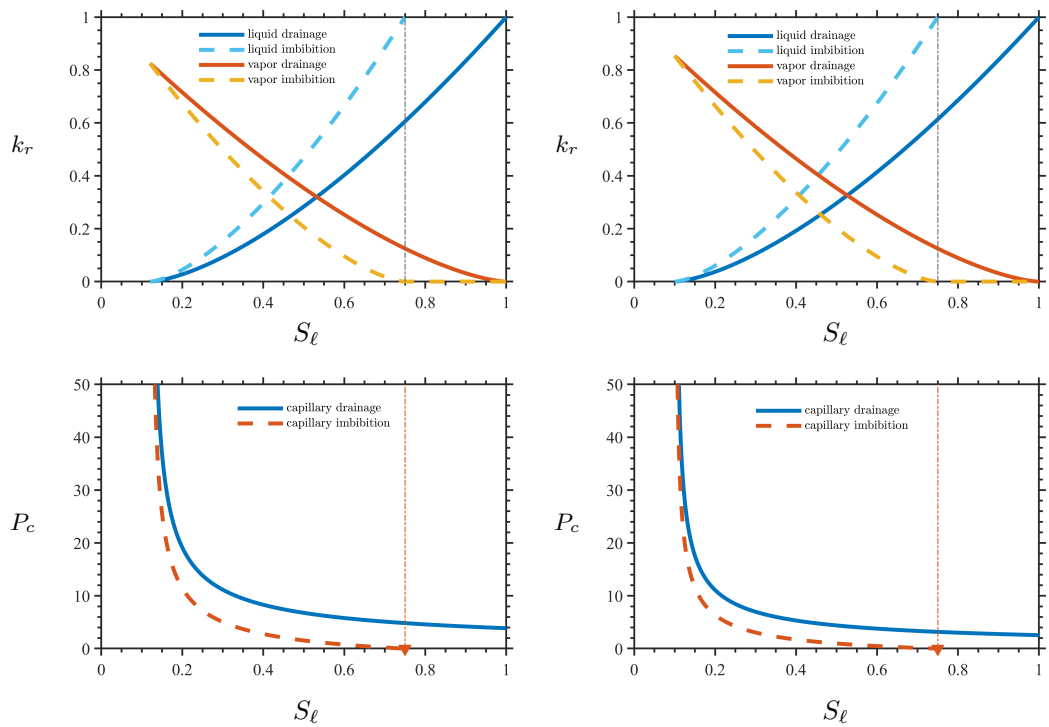

Figure 2: *The saturation functions used in this study based on SPE11 Facies 4 (left column) & 6 (right column) including imbibition.*

2.4. Interface conditions

In the context of geological CO_2 storage, the injected plume migrates upward due to gravity and encounters material interfaces along the way due to the heterogeneous nature of porous media. To motivate the discrete interface-conditions formulation, consider a 1D setting as depicted in Figure 3, where an interface $\Gamma_{\alpha\beta}$ separates two rock types. This interface is located between a lower entry pressure region, Ω_α, and a higher entry pressure region, Ω_β, for the two capillary pressure drainage curves shown in Figure 4. As CO_2 migrates upward toward the interface, it can either invade the top region under specific flow conditions or be trapped below this barrier. These two states depend on the saturation at the interface in the bottom rock region (Ω_α), denoted by $S_v^{\alpha *}$. In this case, the flux across the interface $\Gamma_{\alpha\beta}$ will be of the following possibilities:

1. *CO_2 trapping:* if $S_v^{\alpha *} \leq S_{v,\text{threshold}}^{\alpha *}$, then $S_v^{\beta *} = 0$ and there is no vapor phase flow. The vapor pressure and saturation are discontinuous across the interface.
2. *Counter-current flow:* if $S_v^{\alpha *} > S_{v,\text{threshold}}^{\alpha *}$, then pressure in both phases is continuous across the interface; hence, the capillary pressure is also continuous. The interface saturations are discontinuous and constrained by the capillary pressure at the interface.

Here $S_{v,\text{threshold}}^{\alpha *}$ corresponds to $P_{c,min}^{\beta}$, which is required to invade Ω_β as shown in Figure 4. Mathematically, these dynamics can be formulated by introducing the interface conditions as in Van Duijn et al. (1995). In summary, the two conditions imposed at the discontinuity are the following:

1. *Flux continuity across the interface:* This ensures that the mass flow rate of each phase is conserved at the interface between Ω_α and Ω_β. It reads

$$\boldsymbol{u}_p^\alpha \cdot \boldsymbol{n}_\alpha + \boldsymbol{u}_p^\beta \cdot \boldsymbol{n}_\beta = 0 \quad \text{along} \quad \Gamma_{\alpha\beta} \quad \text{for} \quad p \in \{\ell, v\}, \tag{21}$$

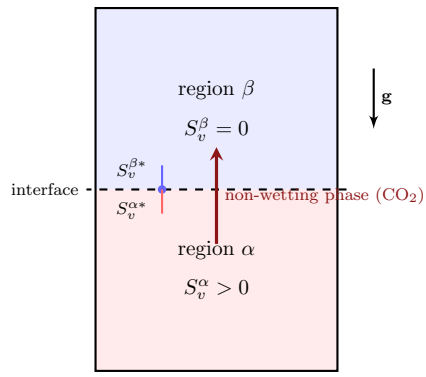

Figure 3: *Schematic of a one-dimensional two-rock-region setup with a material interface at the center, considered in this section. The low-permeability rock region is on the top, and the higher permeability is on the bottom.*

where $\boldsymbol{n}_\alpha = -\boldsymbol{n}_\beta$ is the outward normal to the interface with respect to Ω_α, and similarly for Ω_β. The flux is represented by $\boldsymbol{u}_p^\alpha$, the Darcy velocity for each phase in region Ω_α at the interface, and similarly for Ω_β.

2. *Extended capillary pressure continuity at the interface:* This ensures continuity of phase pressures, hence capillary pressure, is enforced only when both phases are flowing across the interface, not during trapping of any phase. Therefore, we define an extended capillary pressure that treats both states differently, for region Ω_β, as

$$\widetilde{P}_c^{(\beta)} := \min\left(P_{c,max}^{(\alpha)}, \max\left(P_c^{(\beta)}, P_{c,min}^{(\alpha)}\right)\right), \tag{22}$$

and analogously for Ω_α as

$$\widetilde{P}_c^{(\alpha)} := \min\left(P_{c,max}^{(\beta)}, \max\left(P_c^{(\alpha)}, P_{c,min}^{(\beta)}\right)\right). \tag{23}$$

Here $P_{c,min}^{(\alpha)}$ and $P_{c,max}^{(\alpha)}$ denote, respectively, the minimum and the maximum of the capillary pressure function currently active in region Ω_α adjacent to the interface (i.e., the bounding drainage or imbibition curve's range, or the scanning curve's range in the case of hysteresis), and similarly for region Ω_β. Using that, the extended pressure condition enforces a local capillary continuity at the interface with the requirement that

$$\widetilde{P}_c^{(\alpha)}(S^{(\alpha*)}) = \widetilde{P}_c^{(\beta)}(S^{(\beta*)}) \in \left[\max(P_{c,\min}^{(\alpha)}, P_{c,\min}^{(\beta)}),\ \min(P_{c,\max}^{(\alpha)}, P_{c,\max}^{(\beta)})\right] \quad \text{on} \quad \Gamma_{\alpha\beta}, \tag{24}$$

In summary, when one phase is trapped, pressure continuity across the interface exists for the flowing phase. But, the trapped phase pressure can be discontinuous. As a result, capillary pressure and saturations can also be discontinuous. When both phases are flowing, phase pressures, hence capillary pressure, are continuous. Saturations across the interface are discontinuous and related to the unique capillary pressure value as shown in Figure 4(b). While trapping of the non-wetting phase is critical to CO_2 plume migration, these interface conditions also allow for trapping of the wetting phase if $P_{c,max}^\alpha \neq P_{c,max}^\beta$.

3. Numerical Model

We solve the two components' mass conservation equations (1) numerically using a fully implicit time-stepping scheme with a finite-volume spatial discretization. The domain is discretized by a grid of arbitrary structure such that the grid cells conform to the material interfaces between rock regions. The discrete conservation equation for each phase, $p \in \{\ell, v\}$, reads as

$$V_i \frac{(\phi\rho_p S_p)_i^{n+1} - (\phi\rho_p S_p)_i^n}{\Delta t} + \sum_{j\in adj_\alpha(i)} (\rho_p u_p)_{ij}^{n+1} + \sum_{j\in adj_\beta(i)} (\rho_p f_p)_{ij}^{n+1} = V_i(\rho_p q_p)_i^{n+1}, \quad \forall i \in \Omega_\alpha. \tag{25}$$

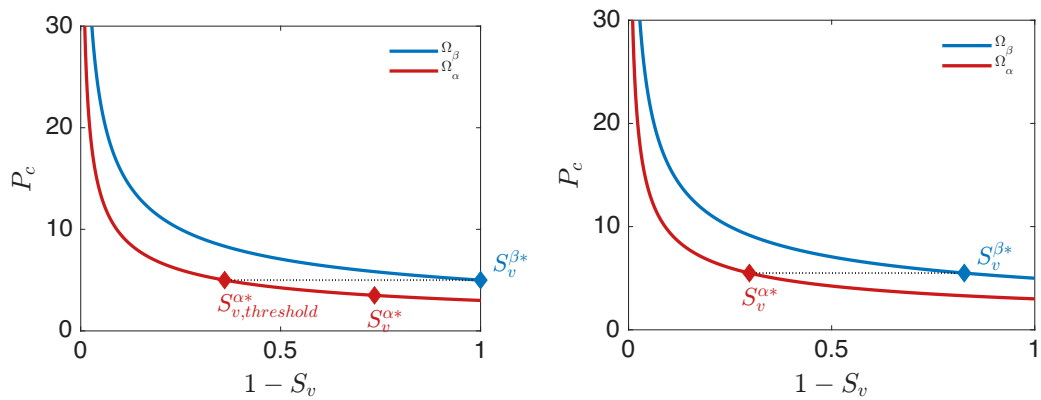

(a) CO_2 is trapped (b) CO_2 is flowing

Figure 4: *Two states in a CO_2 gravity-driven upward migration encountering a capillary entry pressure jump.*

V_i is the bulk volume of cell i. The set of cells that share an interface with cell $i \in \Omega_\alpha$ is partitioned into subsets $adj(i) = adj_\alpha(i) \cup adj_\beta(i)$ where $j \in adj_\alpha(i)$ indicates that $j \in \Omega_\alpha$. On the other hand, $j \in adj_\beta(i)$ indicates that $j \in \Omega_\beta$ with $\Omega_\beta = \Omega_{\setminus\alpha}$, i.e., the cells share a material interface $ij \in \Gamma_{\alpha\beta}$. The volumetric flow between cells is approximated based on a two-point flux approximation (TPFA), and it is treated differently for the homogeneous interfaces using the standard Darcy velocity and heterogeneous interfaces utilizing discrete interface conditions based on a fractional-flow form of the Darcy velocity.

3.1. Homogeneous flux approximation

When $i \in \Omega_\alpha$ and $j \in \Omega_\alpha$, the volumetric flux is defined as

$$u_{p,ij} = T_{ij}\lambda_{p,ij}\Delta\Phi_{p,ij} \quad \text{for} \quad p \in \{\ell, v\}. \tag{26}$$

The rock and geometric transmissibility, T_{ij}, is computed using the one-sided transmissibilities, denoted by $\widehat{T}_{ij}$, as

$$T_{ij} := T_{ji} := (\widehat{T}_{ij}^{-1} + \widehat{T}_{ji}^{-1})^{-1} := \left(\frac{d_{i,(ij)}}{k_i\mathcal{A}_{ij}} + \frac{d_{j,(ji)}}{k_j\mathcal{A}_{ji}}\right)^{-1}. \tag{27}$$

Here k_i (respectively, k_j) is the absolute permeability in cell i (respectively, j) in the direction of the interface, and $d_{i,(ij)}$ (respectively, $d_{j,(ji)}$) is the distance from the center of cell i (respectively, j) to the interface, while $\mathcal{A}_{ij} = \mathcal{A}_{ji}$ is the area of the interface.

We compute the dynamic mobilities and phase densities using upwinding. To do so, we define the difference in phase potentials between neighboring cells as

$$\Delta\Phi_{\ell,ij} := \Phi_{\ell,i} - \Phi_{\ell,j} := \Delta p_{v,ij} - \overline{\rho}_\ell g(\Delta z)_{ij} - (\Delta P_c)_{ij}, \tag{28}$$

$$\Delta\Phi_{v,ij} := \Phi_{v,i} - \Phi_{v,j} := \Delta p_{v,ij} - \overline{\rho}_v g(\Delta z)_{ij}. \tag{29}$$

Here $\overline{\rho}_v$ and $\overline{\rho}_\ell$ represent the arithmetic average of the densities of cells i and j, $(\Delta z)_{ij}$ is the difference between cell centers depths, and $(\Delta P_c)_{ij} = P_c(S_{\ell,i}) - P_c(S_{\ell,j})$.

For the standard Phase-Potential Upwinding (PPU) scheme (Aziz and Settari, 1979; Sammon, 1988), the dynamic terms at the interface (ij) are approximated using the upstream values of the primary unknowns. Here we choose vapor pressure and liquid saturation as primary variables, and we drop their phase subscripts from here onward. So, the phase mobilities are computed as

$$\lambda_{p,ij}(p_i, p_j, S_i, S_j) := \begin{cases} \lambda_p(p_i, S_i) & \text{if} \quad \Delta\Phi_{p,ij} \geq 0 \\ \lambda_p(p_j, S_j) & \text{otherwise,} \end{cases} \tag{30}$$

and similarly the phase densities across the interface are computed as

$$\rho_{p,ij}(p_i, p_j, S_i, S_j) := \begin{cases} \rho_p(p_i) & \text{if} \quad \Delta\Phi_{p,ij} \geq 0 \\ \rho_p(p_j) & \text{otherwise.} \end{cases} \tag{31}$$

We will refer to this numerical scheme as PPU. At heterogeneous interfaces, PPU honors flux continuity but doesn't not satisfy a discrete form of capillary pressure continuity (24). We observe that PPU does converge to the correct solution in the limit of spatial grid refinement. But significant errors occur on coarse grids where cell-average saturations and the associated capillary pressures yield inaccurate approximations to interface values.

3.2. Heterogeneous flux approximation using discrete interface conditions

When the two cells belong to different rock regions, i.e., $i \in \Omega_\alpha$ and $j \in \Omega_\beta$, a more accurate volumetric flux can be computed using a discrete version of the interface conditions of Section (2.4). The formulation follows Van Duijn et al. (1995) and builds on the discretization presented in Cancès (2009); Hamon et al. (2018); Alali et al. (2021); Bosma (2021). In this work, we introduce a single unknown per interface, which is the interface capillary pressure $P_{c,ij} \in \big[\min(P^{(\alpha)}_{c,\min}, P^{(\beta)}_{c,\min}),\ \max(P^{(\alpha)}_{c,\max}, P^{(\beta)}_{c,\max})\big]$. From $P_{c,ij}$ we define the interface saturation pair $(S^{(\alpha*)}_{ij}, S^{(\beta*)}_{ij})$ using the capillary pressure inverse for each side, so that the interface saturations become functions of $P_{c,ij}$:

$$\begin{aligned} S^{(\alpha*)}_{ij} &= \big(P^{(\alpha)}_{c,i}\big)^{-1}\Big(\min\big(P^{(\alpha)}_{c,\max},\ \max\big(P_{c,ij},\ P^{(\alpha)}_{c,\min}\big)\big)\Big), \\ S^{(\beta*)}_{ij} &= \big(P^{(\beta)}_{c,j}\big)^{-1}\Big(\min\big(P^{(\beta)}_{c,\max},\ \max\big(P_{c,ij},\ P^{(\beta)}_{c,\min}\big)\big)\Big). \end{aligned} \tag{32}$$

We compute the numerical flux by finding the $P_{c,ij}$ value that satisfies volumetric flux continuity in fractional-flow form. To do this, we first define the total volumetric velocity, $u_{T,ij}(p_i, p_j, S_i, S_j) := u_{\ell,ij} + u_{v,ij}$, that is not a function of $P_{c,ij}$, where the phase fluxes are evaluated with PPU as outlined in the previous section. Phase flux continuity is then expressed as:

$$f^{\alpha}_{\ell,ij}\big(u_{T,ij}, p_i, S_i, P_{c,ij}\big) = -f^{\beta}_{\ell,ji}\big(u_{T,ji}, p_j, S_j, P_{c,ij}\big). \tag{33}$$

Here $f^{\alpha}_{\ell,ij}$ is approximated as a homogeneous, one-sided flux at the interface as:

$$f^{\alpha}_{\ell,ij} = \frac{\widehat{\lambda}_{\ell,ij}}{\widehat{\lambda}_{\ell,ij} + \widehat{\lambda}_{v,ij}} u_{T,ij} + \widehat{T}_{ij}\frac{\widehat{\lambda}_{\ell,ij}\widehat{\lambda}_{v,ij}}{\widehat{\lambda}_{\ell,ij} + \widehat{\lambda}_{v,ij}}(\rho_v - \rho_\ell) g (\Delta\widehat{z})_{ij} - \widehat{T}_{ij}\frac{\widehat{\lambda}_{\ell,ij}\widehat{\lambda}_{v,ij}}{\widehat{\lambda}_{\ell,ij} + \widehat{\lambda}_{v,ij}}(\Delta\widehat{P}_c)^{(\alpha)}_{ij}, \tag{34}$$

where $\widehat{T}_{ij}$ is a one-sided transmissibility, and $\Delta\widehat{z}_{ij}$ is the depth difference between the cell center and the interface. The third term involves a capillary pressure difference, $(\Delta\widehat{P}_c)^{(\alpha)}_{ij} = P^{(\alpha)}_{c,i}\big(S_i\big) - P^{(\alpha)}_{c,i}\big(S^{(\alpha*)}_{ij}\big)$, using the currently-active capillary pressure curve selected by the hysteresis mode of cell i, i.e. its cell-centered saturation and historical saturation extrema. Hence $(\Delta\widehat{P}_c)^{(\alpha)}_{ij}$ reduces to $P^{(\alpha)}_{c,i}(S_i) - P_{c,ij}$ whenever the interface capillary pressure lies within the range of region α as defined in (32). Lastly, the mobilities in (34) are evaluated at the upstream state between the cell center and the interface, i.e., $\widehat{\lambda}_{p,ij} := \lambda_{p,ij}(p_i, p_i, S_i, S^{(\alpha*)}_{ij})$, according to the consistent phase upwinding method by Brenier and Jaffré (1991). Also, $f^{\beta}_{\ell,ji}$ is the liquid fractional-flow flux at the interface approximated as a homogeneous one-sided flux on the β side, and it is defined analogously.

Equation (33) thus ensures discrete mass-flow-rate continuity of the liquid across the interface, because the liquid density is fixed and upwinded using (31) at each interface. Moreover, because the total velocity does not change, equation (33) simultaneously yields conservation of the vapor-phase mass flow rate. By the use of the extended capillary pressure definition to solve a scalar nonlinear equation, we avoid variable switching. This improves efficiency and allows better handling of different types of capillary pressure curves, including bounding and scanning hysteresis curves. Moreover, Bosma (2021) showed that this formulation can be extended to three-phase systems. We summarize the numerical procedure for solving (33) in Algorithm 1. By numerically solving the nonlinear scalar mass conservation equation at the interface for the single primary unknown, which is a cheap scalar solve in comparison to the global nonlinear system, we obtain the local flux and the derivatives of the local flux with respect to the cell-centered variables, which are the main requirements for the global numerical solve.

Algorithm 1: Solution algorithm for the local nonlinear problem (33).

Data: Cell-centered variables of phase saturation S_i and S_j, and total volumetric flux $u_{T,ij}$.

Result: Phase volumetric fluxes $f_{p,ij}^{n+1}$ and $f_{p,ji}^{n+1}$, along with the flux derivatives with respect to the cell-centered primary variables (p_i, p_j, S_i, S_j).

Initial guess:

In the first timestep:

$P_{c,ij} \longleftarrow \frac{1}{2}(P_{c,i} + P_{c,j})$

In a subsequent timestep, k:

$P_{c,ij}^{k} \longleftarrow P_{c,ij}^{k-1}$

Newton loop:

for $\nu = 1, \ldots, n_{max}^{loc}$ **do**

A) Evaluate the local residual and its derivative

$$S_{ij}^{(\alpha*)} \longleftarrow g_\alpha(P_{c,ij}) = \left(P_{c,i}^{(\alpha)}\right)^{-1}\Big(\min\left(P_{c,\max}^{(\alpha)},\ \max\left(P_{c,ij},\ P_{c,\min}^{(\alpha)}\right)\right)\Big)$$

$$S_{ji}^{(\beta*)} \longleftarrow g_\beta(P_{c,ij}) = \left(P_{c,j}^{(\beta)}\right)^{-1}\Big(\min\left(P_{c,\max}^{(\beta)},\ \max\left(P_{c,ij},\ P_{c,\min}^{(\beta)}\right)\right)\Big)$$

$$R_{loc} \longleftarrow f_{\ell,ij}^{n+1}\left(u_{T,ij}, S_i, S_{ij}^{(\alpha*)}\right) + f_{\ell,ji}^{n+1}\left(u_{T,ji}, S_j, S_{ij}^{(\beta*)}\right)$$

$$J_{loc} \longleftarrow \frac{\partial R_{loc}}{\partial P_{c,ij}} = \frac{\partial f_{\ell,ij}^{n+1}}{\partial S_{ij}^{(\alpha*)}}\frac{\partial g_\alpha}{\partial P_{c,ij}} + \frac{\partial f_{\ell,ji}^{n+1}}{\partial S_{ij}^{(\beta*)}}\frac{\partial g_\beta}{\partial P_{c,ij}}$$

where $\dfrac{\partial g_\alpha}{\partial P_{c,ij}} = \left[\dfrac{\partial P_{c,ij}}{\partial \widetilde{P}_{c,i}^{(\alpha)}}\dfrac{\partial \widetilde{P}_{c,i}^{(\alpha)}}{\partial S_{ij}^{(\alpha*)}}\right]^{-1}$ and $\dfrac{\partial g_\beta}{\partial P_{c,ij}} = \left[\dfrac{\partial P_{c,ij}}{\partial \widetilde{P}_{c,j}^{(\beta)}}\dfrac{\partial \widetilde{P}_{c,j}^{(\beta)}}{\partial S_{ij}^{(\beta*)}}\right]^{-1}$

B) Check convergence

if $|R_{loc}/(\phi_i V_i + \phi_j V_j)| \times \Delta t < \epsilon_{local}$ **then**

  break

C) Update the capillary pressure

$P_{c,ij} \longleftarrow P_{c,ij} - J_{loc}^{-1} R_{loc}$

end

Compute global derivatives with respect to cell-centered variables:

$$\frac{\partial}{\partial \tau_i}\left[f_{p,ij}^{n+1}\left(u_{T,ij}, S_i, S_{ij}^{(\alpha*)}\right)\right] \longleftarrow \frac{\partial f_{p,ij}}{\partial u_{T,ij}}\frac{\partial u_{T,ij}}{\partial \tau_i} + \frac{\partial f_{p,ij}}{\partial S_i}\frac{\partial S_i}{\partial \tau_i} + \frac{\partial f_{p,ij}}{\partial S_{ij}^{(\alpha*)}}\frac{\partial g_\alpha}{\partial P_{c,ij}}\frac{\partial P_{c,ij}}{\partial \tau_i}$$

$$\frac{\partial}{\partial \tau_j}\left[f_{p,ij}^{n+1}\left(u_{T,ij}, S_i, S_{ij}^{(\alpha*)}\right)\right] \longleftarrow \frac{\partial f_{p,ij}}{\partial u_{T,ij}}\frac{\partial u_{T,ij}}{\partial \tau_j} + \frac{\partial f_{p,ij}}{\partial S_{ij}^{(\alpha*)}}\frac{\partial g_\alpha}{\partial P_{c,ij}}\frac{\partial P_{c,ij}}{\partial \tau_j}$$

4. Numerical Solution

For the fully-implicit solution procedure of the discretized mass conservation equations (25), we first cast both equations for each phase, $p \in \{\ell, v\}$ in residual form:

$$R_{p,i} = V_i \frac{(\phi\rho_p S)_i^{n+1} - (\phi\rho_p S)_i^n}{\Delta t} + \sum_{j \in adj_\alpha(i)} (\rho_{p,ij} u_{p,ij})^{n+1} + \sum_{j \in adj_\beta} (\rho_{p,ij} f_{p,ij})^{n+1} - V_i (\rho_p \tilde{q}_p)_i^{n+1} = 0, \quad \forall i \in \Omega_\alpha, \tag{35}$$

where the homogeneous-interface flux $u_{p,ij}$ is given by (26) and the heterogeneous-interface flux $f_{p,ij}$ is obtained from the discrete interface conditions of Section 3.2, in the one-sided fractional-flow form (34) in the case of PPU-C. This yields a nonlinear system of equations $\boldsymbol{R}(\boldsymbol{X}^{n+1}) = \boldsymbol{0}$ where $\boldsymbol{X} = [p_v, S_\ell]^T$ for each cell. Then, we linearize the system and solve for the pressure and saturation of each cell using the Newton-Krylov method as implemented in GEOS (Settgast et al., 2024):

$$\boldsymbol{J}^\nu \delta \boldsymbol{X} = -\boldsymbol{R}^\nu, \qquad \boldsymbol{X}^{\nu+1} = \boldsymbol{X}^\nu + \gamma \delta \boldsymbol{X}, \tag{36}$$

where $\boldsymbol{J}$ is the Jacobian matrix associated with the nonlinear global residual, $\boldsymbol{R}$, and $\gamma \in (0, 1]$ is a line search parameter. Global convergence is achieved when

$$\|R_{p,i}\|_2 / (\phi_i \rho_{p,i} V_i) < \epsilon_{\text{global}} \quad \forall p \in \{\ell, v\}. \tag{37}$$

is satisfied for all cells. We set the local nonlinear solver tolerance, ϵ_{local} of Algorithm 1, so that the global nonlinear solution tolerance, ϵ_{global}, is at least 2 orders of magnitude stricter to ensure no adverse impact on global convergence. Moreover, we solve the local scalar nonlinear equation at every heterogeneous interface using a safeguarded Newton method combined with bisection bracketing and damping. This scalar nonlinear solver is cheap and solving it for multiple interfaces is easily parallelizable, making it a good fit for HPC frameworks. Lastly, to compute the capillary pressure inverse, we rely on analytical inverse forms for capillary pressure curves such as Brooks and Corey (1964), whereas for tabulated capillary pressure curves, we use piecewise linear interpolation. However, for hysteresis scanning curves that do not have a closed-form equation, we rely on a numerical inverse computed using a safeguarded Newton method with bracketing and damping. Regarding the Krylov-based linear solver, GEOS employs a preconditioned Krylov method with a multigrid reduction preconditioner (MGR) provided by the *hypre* library, more details can be found in Settgast et al. (2024); Bui et al. (2021); Kachuma et al. (2026).

5. Numerical Examples

In this section, we present four numerical examples in increasing order of complexity. The table below shows a summary of the rock and fluid properties used in Examples 1 and 2, based on fluid and rock properties of an isothermal, incompressible, and immiscible version of SPE11:

Table 1: *Fluid and rock properties for Examples 1 and 2.*

Rock Property	Facies 6 (bottom)	Facies 4 (top)
Permeability (m^2)	2.00×10^{-12}	5.00×10^{-13}
Immobile Saturation $S_{\ell,c}$	0.1	0.12
Entry pressure (Pa)	2560	3870
Fluid Property	CO_2	Water
Density (kg/m^3)	850.2	998.3
Viscosity (Pa.s)	8.18×10^{-5}	5.11×10^{-4}

5.1. Example 1: 1D gravity segregation

This 1D gravity segregation example depicts a post-injection CO_2 storage period. For simplicity, we consider a vertical column of dimensions 5 m × 5 m × 10 m consisting of two layers separated by a horizontal interface at the center ($z = 5$ m), as sketched in Fig. 5(a). The bottom layer corresponds to SPE-11B Facies 6 and the top layer to Facies 4, with the bottom permeability being four times higher than the top. The domain is initially saturated with water except for the bottom fifth of the column, which is saturated with CO_2 at ($S_v = 0.89$) which is slightly greater than the connate water saturation. There is no source or sink term such that gravity and capillarity are therefore the only driving forces of the flow. Under gravity, the lighter CO_2 migrates upward while water travels to the bottom. Moreover, we consider two sets of saturation functions, with and without hysteresis. This configuration admits an analytical steady-state solution when there is no hysteresis, as explained in Appendix A, and we use it as a benchmark. Thus, the analytical profile shown in Fig. 5(b) provides a reference against which we compare the converged numerical solutions.

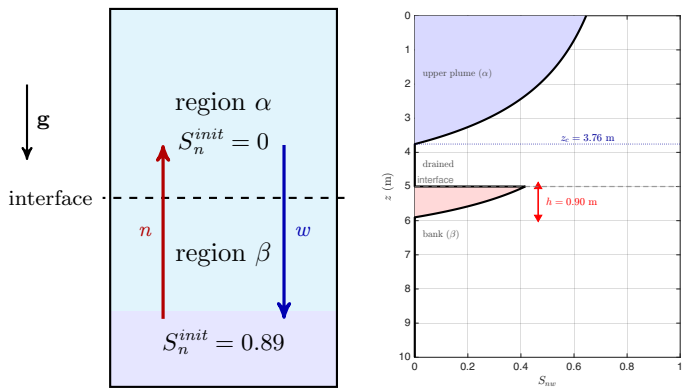

(a) 1D schematic (b) Steady-state solution

Figure 5: *Example 1 setup in (a): 1D vertical column of two layers separated by a capillary interface at the center with the bottom fifth initialized with CO_2, and the steady-state analytical solution in (b).*

5.1.1. Results

We compare PPU and PPU-C at grid resolutions of $N_z = 10$, 20, 40, 100, and 200 cells in the vertical direction against the corresponding highly refined grid ($N_z = 10000$) solution at two time instances. We also include the analytical solution as a reference for the steady-state solutions. The saturation profiles obtained with the two numerical schemes until steady state are shown in Figure 6.

After 7 days, we see that the standard PPU scheme predicts early invasion of the top region for small N_z, i.e., for coarser levels of spatial refinement. At steady-state, we see that PPU significantly under-predicts the trapping for coarser levels of spatial refinement. For instance, for $N_z = 10$, PPU predicts no trapping at all, compared to the analytical 5.5 m^3. This under-prediction is reduced upon spatial refinement but with a slow convergence to the reference solution as N_z is increased.

Figure 7(a) shows the L_2 error norm of the CO_2 volume fraction in the whole domain at steady state as a function of grid resolution. PPU-C converges faster than PPU. Figure 7(b) shows the total trapped CO_2 volume (below the interface) versus grid resolution. PPU-C captures the trapped volume accurately even on very coarse grids, while PPU requires substantial refinement to approach the reference value.

5.1.2. Results with hysteresis

We repeat this test case, now accounting for the path dependence of the saturation functions shown in Fig. 2. Including hysteresis allows us to estimate not only capillary trapping due to capillary heterogeneity, but also residual trapping, so the trapped amount is now attributed to both mechanisms.

Figure 8 compares saturation profiles at two time instances for different grid-refinement levels for PPU and PPU-C. With coarse PPU, the plume invades the top zone earlier than the other cases, whereas coarse PPU-C maintains accurate interface behavior. As in the no-hysteresis example, the PPU solution

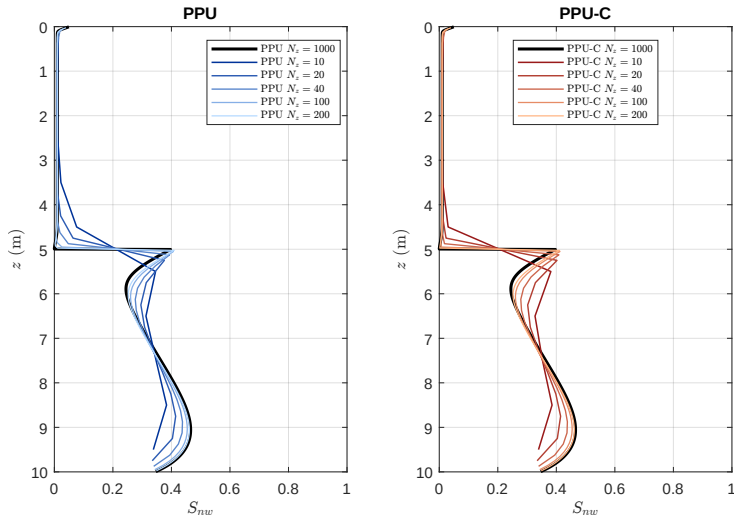

(a) After 7 days

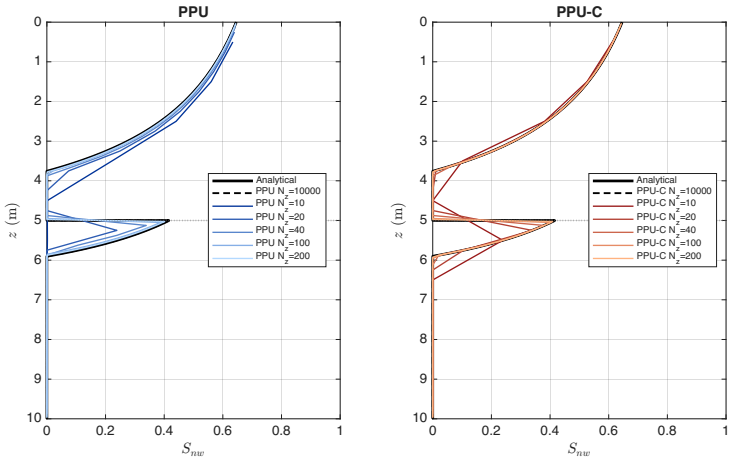

(b) At steady-state

Figure 6: *Example 1 (no hysteresis): CO_2 saturation profiles for PPU and PPU-C at different resolutions, compared with spatially refined solutions at two times: when the plume first invades the top zone, as predicted by PPU in (a), and at steady state in (b) which includes the analytical solution.*

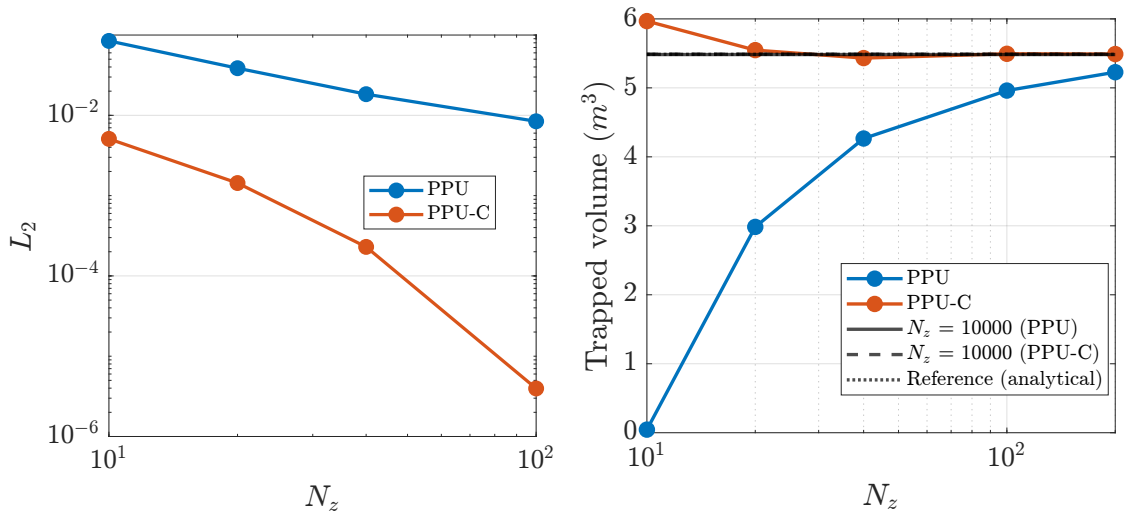

(a) L_2 error norm

(b) Total trapped CO_2 volume

Figure 7: *Example 1 (no hysteresis): L_2 error norm of CO_2 volume fraction at steady state vs. number of cells N_z in (a). Total trapped CO_2 volume below the interface vs. N_z in (b). The black lines indicate the references.*

approaches the reference solution relatively slowly under refinement at any fixed time, while PPU-C converges rapidly.

In summary, at $t = 20$ days, comparing the volume of gas that has crossed the interface between the coarse solutions, PPU overestimates by about 75% relative to the highly-refined solution value of 1.192 m^3. PPU-C predicts an overestimation of about 17%. When comparing the total trapped CO_2 volume below the interface between the coarse solutions, PPU underestimates it by about 3% relative to the highly-refined solution value of 6.218 m^3. PPU-C predicts an underestimation of less than 1%.

5.1.3. Computational performance

Table 2 summarizes the computational performance of PPU and PPU-C for the 1D case on a single MPI rank, both without and with hysteresis. The nonlinear behavior of the two schemes in all four cases is essentially identical. They take the same number of time steps and timestep cuts, and their nonlinear iteration counts agree to within 1%. In this example, the cost of the local interface solver is fully exposed due to the similar global nonlinear convergence performance, and PPU-C is 8–9% slower overall without hysteresis and slightly slower than that (13–14%) with hysteresis, with the overhead concentrated in the residual and Jacobian assembly. This additional overhead in the cases with hysteresis could be attributed to the additional nested nonlinear problem solved to obtain the capillary pressure inverse for the scanning hysteretic curves. Also, the nonlinear performance shows timestep cuts in the refined cases with hysteresis due to the additional nonlinearities from flow reversal, which are encountered in both schemes.

Table 2: *Example 1: Computational performance comparison without and with hysteresis (1 MPI rank). Hysteresis columns are taken at $t = 150$ days, and the other columns are at steady-state ($t = 1000$ days).*

	Without hysteresis				With hysteresis			
	$N_z = 10$		$N_z = 1000$		$N_z = 10$		$N_z = 1000$	
Metric	PPU	PPU-C	PPU	PPU-C	PPU	PPU-C	PPU	PPU-C
Time steps	1,027	1,027	100,031	100,021	161	161	13,419	13,420
Timestep cuts	0	0	0	0	0	0	29	29
NL iterations	1,142	1,142	119,010	119,130	273	276	32,297	32,167
Discarded NL	0	0	0	0	0	0	1,160	1,160
Run time (s)	9.9	10.8	1,083	1,170	3.95	4.51	464.7	523.7

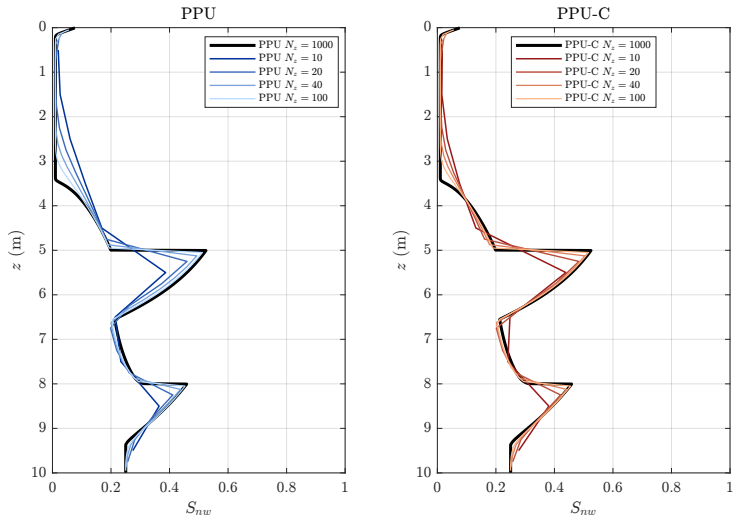

(a) After 20 days

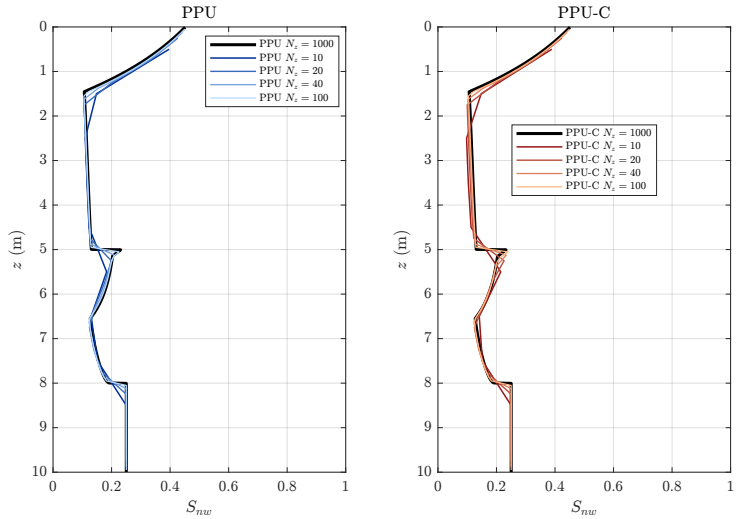

(b) After 130 days

Figure 8: *Example 1 (hysteresis): CO_2 saturation profiles at two times: when the plume first invades the top zone and reaches the top boundary, as predicted by PPU in (a), and near steady state in (b). The black lines indicate the highly refined solutions.*

5.2. Example 2: 3D gravity segregation

We now extend the study of the accuracy of the numerical schemes in a multidimensional porous medium and shed light on their efficiency in cases with multiple interfaces. We extend Example 1 to three dimensions. The domain is of size 10 m × 6 m × 10 m with the same two-layer configuration and interface at $z = 5$ m. The domain is initially fully saturated with water, with a small CO_2 plume of the size 4 m × 4 m × 4 m placed at one bottom corner as shown in Figure 9. The plume migrates under gravity and spreads laterally, testing interface conditions in a multidimensional setting with multiple local solves.

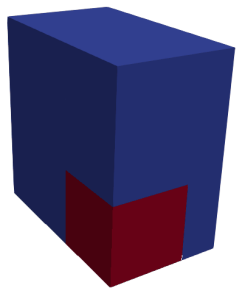

Figure 9: *Example 2 setup: 3D domain with two layers and initial CO_2 plume at the corner.*

5.2.1. Results

Figures 10(a) and 10(b) show the L_2 error norm and trapped volume as functions of grid resolution, along with the corresponding highly refined estimates, analogous to the 1D case. PPU-C maintains its accuracy advantages in 3D. Figure 11 also shows the 3D saturation domain at the end of the simulation for coarse PPU and PPU-C results, compared with their corresponding fine solutions.

On the other hand, the simulation of the same case with hysteresis yields results similar to the 1D case with hysteresis. Figure 12 compares the 3D saturation fields with hysteresis at $t = 3$ days for PPU-C and PPU on a coarse grid (5 × 3 × 10 cells) alongside refined PPU and PPU-C cases (40 × 24 × 270 cells). Similar to the 1D case, PPU allows premature invasion of the top zone. In fact, at $t = 6$ days, comparing the volume of gas that has crossed the interface among the coarse solutions, PPU predicts an overestimation of about 32% relative to the highly refined simulation result of 4.950 m^3. PPU-C predicts an underestimation of about 8%.

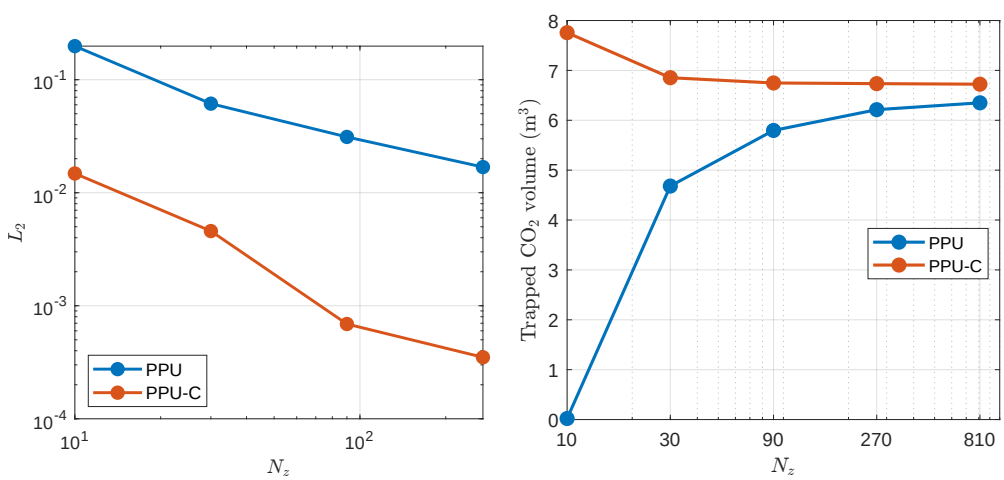

(a) L_2 error norm (b) Total trapped CO_2 volume

Figure 10: *Example 2 (no hysteresis): L_2 error norm of CO_2 volume fraction at steady state vs. grid resolution in (a). Total trapped CO_2 volume below the interface vs. grid resolution in (b).*

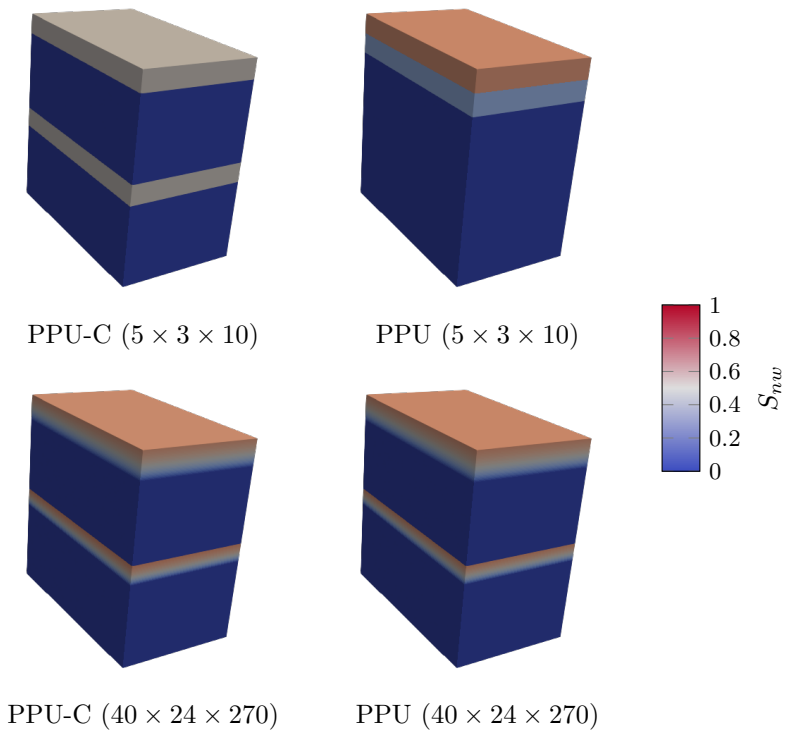

Figure 11: *Example 2 (no hysteresis): Steady-state 3D saturation fields on a coarse grid (top row) compared with refined solutions (bottom row), for PPU-C (left column) and PPU (right column).*

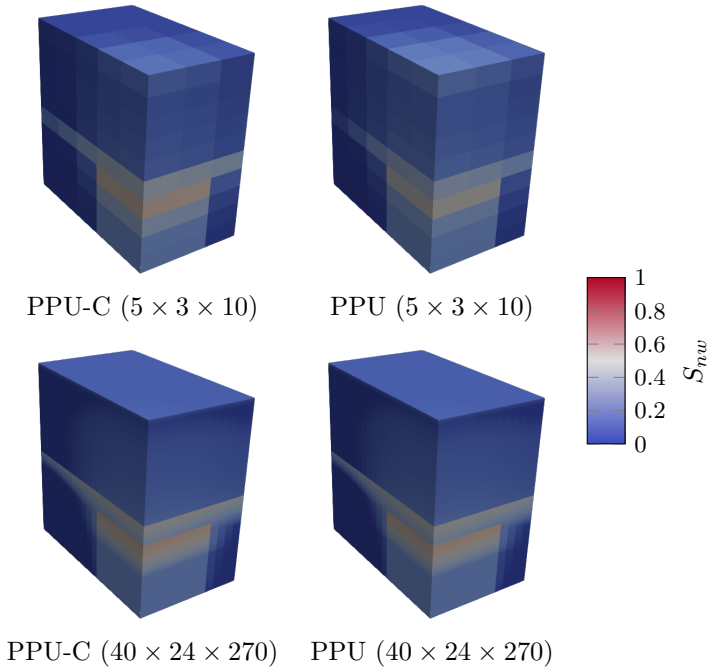

Figure 12: *Example 2 (hysteresis): 3D saturation fields on a coarse grid (top row) compared with refined solutions (bottom row) after 4 days*

5.2.2. Computational performance

Table 3 summarizes the computational performance of PPU and PPU-C for the 3D case using 60 MPI ranks. In contrast to the 1D case, where the nonlinear behavior of the two schemes is identical, and the interface solver overhead is fully exposed, PPU-C improves nonlinear convergence here at every resolution without hysteresis, especially on the finer grids, with far fewer timestep cuts and discarded iterations. Even on the coarse $10 \times 6 \times 20$ grid, where the schemes do not resolve the same solution (Section 5.2.1), the slightly better convergence of PPU-C is already sufficient to offset the interface solver overhead, and the two run times are nearly identical. On the finer grids, where the solutions agree, the improved robustness dominates, and PPU-C achieves speedups of 2.8× and 2.0× on the $20 \times 12 \times 90$ and $40 \times 24 \times 270$ grids, respectively. In the hysteresis cases, PPU-C shows a slight improvement in nonlinear convergence, but both schemes are affected by flow-reversal nonlinearities, which dominate even more in this 3D setting, resulting in similar run times.

Table 3: *Example 2: Computational performance comparison without and with hysteresis (60 MPI ranks). Hysteresis columns are taken at $t = 10$ days, and the other columns are at steady-state ($t = 100$ days).*

	Without hysteresis						With hysteresis					
	$10 \times 6 \times 30$		$20 \times 12 \times 90$		$40 \times 24 \times 270$		$5 \times 3 \times 10$		$20 \times 12 \times 90$		$40 \times 24 \times 270$	
Metric	PPU	PPU-C	PPU	PPU-C	PPU	PPU-C	PPU	PPU-C	PPU	PPU-C	PPU	PPU-C
Time steps	176	167	581	246	1,647	414	107	95	686	668	3,760	3,608
Timestep cuts	1	0	44	2	247	14	0	0	33	31	138	91
NL iterations	403	380	1,864	1,120	5,923	2,330	211	205	6,094	6,007	36,679	36,520
Discarded NL	20	0	880	40	4,940	280	0	0	660	620	2,760	1,820
Run time (s)	8.18	8.02	128.8	45.8	1,912.6	942.9	10.57	10.37	316.7	321.9	5,154	5,109

5.3. Two-dimensional domain with multiple capillary barriers

In this third example, we increase the geometric complexity by considering a two-dimensional domain of size 100 m × 100 m containing multiple randomly distributed capillary barriers, with a configuration inspired by Hamon et al. (2016), as shown in Figure 13. The barriers are low-permeability, high-entry-pressure lenses based on Facies 4, embedded in a higher-permeability background rock based on Facies 6, as per Table 1. We initialize the problem with a 10 m band at the bottom of the domain saturated with CO_2 at slightly greater than the connate water saturation ($S_v = 0.89$), so that the CO_2 migrates upward under buoyancy through the barrier field during the post-injection period. We also increase the rock and fluid complexity by varying the fluid density and viscosity with pressure, and by using analytical capillary pressure curves as per (5) rather than the bounded versions used in SPE11.

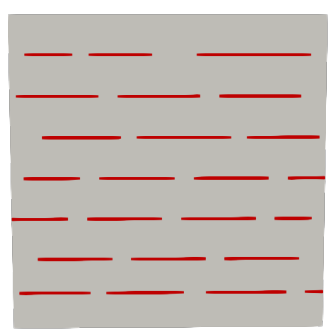

Figure 13: *Example 3: 2D domain setup*

We compare the standard PPU and PPU-C schemes on the same 100×100 grid. Figure 14 shows the vapor saturation S_v at $t = 5$, 10, 45, and 125 days. At early times ($t = 5$ days), the two schemes

produce similar plume shapes as CO_2 begins to rise and accumulate beneath the lowermost barriers. As the simulation progresses, the difference between the two schemes becomes pronounced and the two schemes produce different final solutions.

5.3.1. Computational performance

Table 4 summarizes the computational performance of PPU and PPU-C for the 2D case with random barriers using 25 MPI ranks; as discussed in the previous section, the two schemes converge to different solutions here, so the timings should be read with this in mind. Neither scheme requires timestep cuts, and the two take identical number of time steps; PPU-C requires about 2% more nonlinear iterations and a 7% longer run time. Since the PPU solution reaches steady-state sooner, the PPU-C overhead is attributed to both the additional iterations and the interface computation.

Table 4: *Example 3: Computational performance comparison (25 MPI ranks).*

	100×100	
Metric	PPU	PPU-C
Time steps	12,519	12,519
Timestep cuts	0	0
NL iterations	12,604	12,812
Discarded NL	0	0
Run time (s)	2,199	2,349

5.4. Example 4: SPE-11B benchmark (2D cross-section)

5.4.1. Problem setup

We conclude with a field-scale two-dimensional domain from the SPE11 Comparative Solution Study, case B (Nordbotten et al., 2024). The domain is of size 8.4 km $\times$ 1.2 km and contains multiple facies with distinct capillary pressure and relative permeability curves, providing numerous capillary interfaces. We convert the problem to isothermal, immiscible, two-phase flow with compressibility and model it without hysteresis. Well 1 injects CO_2 for 50 years; Well 2 injects from year 25 to year 50. The simulation continues for 1000 years.

5.4.2. Results

We compare PPU and PPU-C on a grid of 420×60 cells. Figure 14 shows the CO_2 saturation field for PPU-C and the difference map (PPU-C $-$ PPU) at four time instances: 30, 50, 100, and 1000 years. The results show that PPU invades the top layers faster near the injector in the center of the domain while PPU-C maintains higher trapping in the lower layers. Also, in the post-injection phase, the plume extends farther to the right in the domain for PPU, whereas it migrates towards the left for PPU-C.

5.4.3. Computational performance

Table 5 summarizes the computational performance of PPU and PPU-C for the SPE11B case using 10 MPI ranks. The nonlinear performance of the two schemes is comparable, with PPU-C requiring marginally fewer time steps, nonlinear iterations, and discarded iterations. The interface solver overhead is therefore not amortized, and PPU-C is about 25% slower overall, reflecting a per-iteration cost increase larger than in the previous examples, consistent with the larger fraction of interfaces in the heterogeneous SPE11B facies description.

6. Conclusion

In this work, we presented a fully implicit finite-volume scheme enhanced with discrete interface conditions (PPU-C) for modeling capillary-dominated multiphase flow in heterogeneous porous media, with direct application to geological CO_2 storage. The scheme enforces local capillary dynamics at

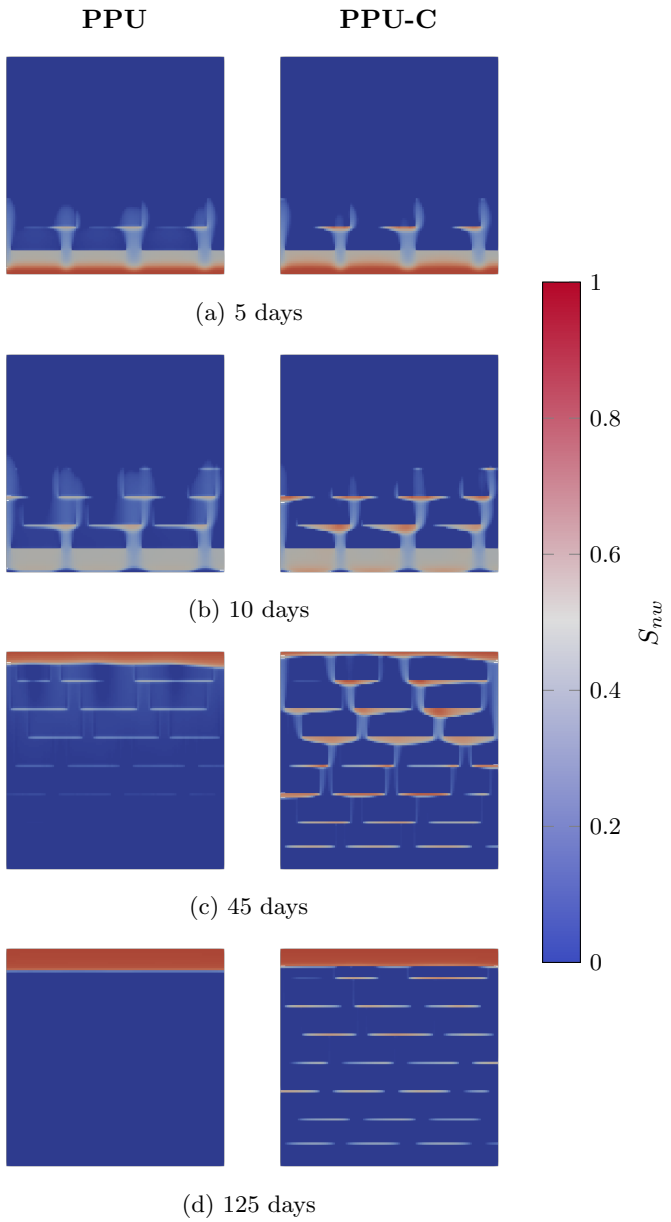

Figure 14: *Example 3: PPU vapor saturation (left column) and PPU-C (right column) on a* 100×100 *grid at 5, 10, 45, and 125 days.*

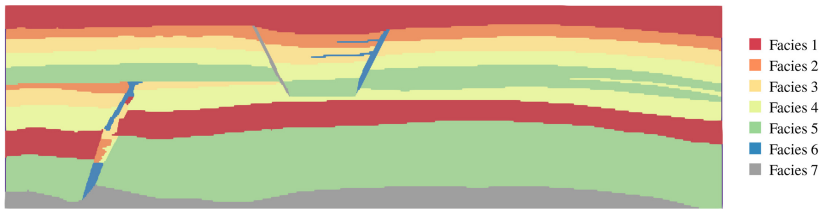

Figure 15: *Example 4: SPE-11B domain geometry and facies distribution (Nordbotten et al., 2024).*

Table 5: *Example 4: Computational performance comparison (10 MPI ranks).*

	420×60	
Metric	PPU	PPU-C
Time steps	1,525	1,487
Timestep cuts	45	43
NL iterations	3,020	2,967
Discarded NL	675	645
Run time (s)	258.5	324

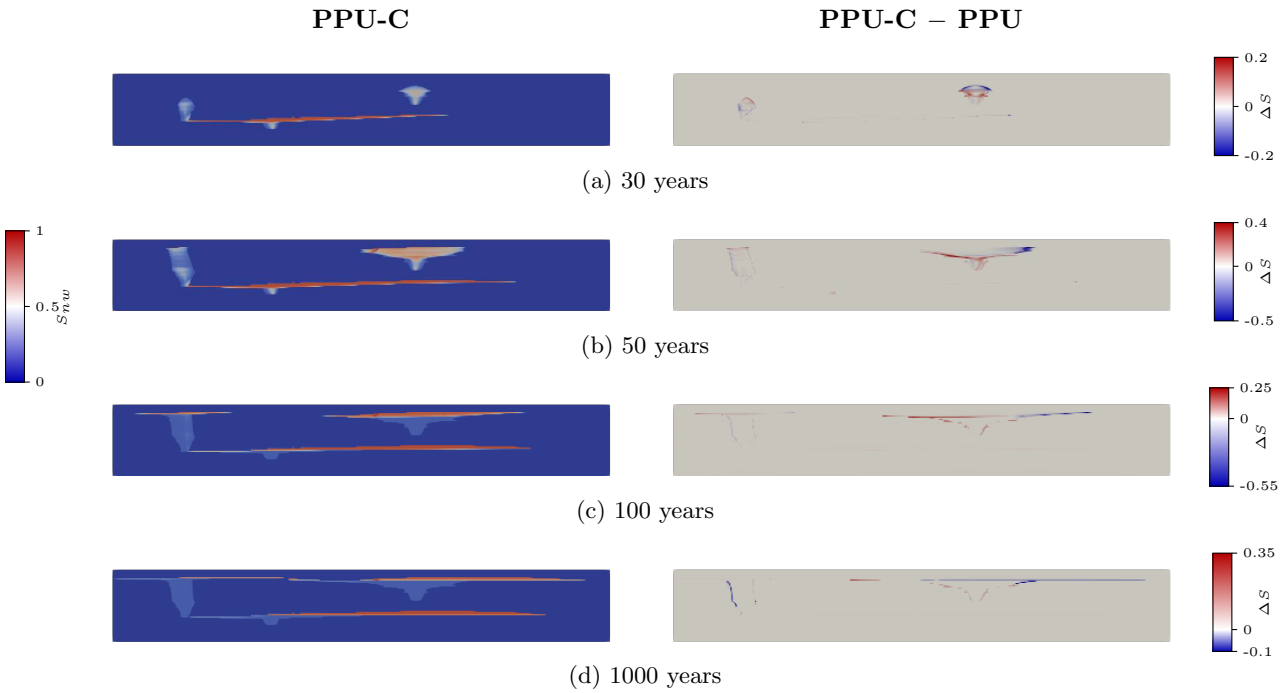

Figure 16: *Example 4: PPU-C CO_2 saturation (left column, scale 0 to 1) and difference map PPU-C − PPU (right column, with an individual scale for each time) on a 420×60 grid at 30, 50, 100, and 1000 years. Red indicates where PPU-C predicts higher CO_2 saturation than PPU; blue indicates lower.*

material interfaces by introducing an interface capillary pressure as a local primary variable, which is solved via a local nonlinear solver at each material interface during the global flux and Jacobian assembly. The formulation was extended to incorporate capillary pressure and relative permeability hysteresis, and implemented within the open-source GEOS simulation framework. The conclusions of this work can be summarized as follows:

1. Our observations are consistent with recent research findings on the importance of accounting for capillary heterogeneity in determining the CO_2 migration path and the ultimate amount trapped in GCS applications, and how this presents a challenge for large-scale simulations (Ni et al., 2025; Zhang et al., 2025). We showed that standard PPU reservoir simulation models always underestimate the final securely trapped amount unless excessive grid refinement is performed.
2. We showed that using interface conditions within the PPU-C numerical simulation scheme is a very effective strategy to reduce this capillary-heterogeneity error for practical grids. In the presented numerical spatial convergence results, PPU-C consistently produces solutions that are an order of magnitude more accurate than those of standard PPU.
3. PPU-C computational overhead compared to PPU never exceeded 25% in the presented numerical examples. Moreover, when the nonlinear solver is challenged, as in high-resolution 3D simulations where PPU and PPU-C results coincide, the improved nonlinear convergence of PPU-C yields speedups of up to more than 2.0× over PPU.
4. Beyond resolving capillary heterogeneity trapping physics, it is critical to account for capillary pressure and relative permeability hysteresis in GCS simulation, since a significant portion of the securely stored CO_2 is attributed to residual trapping.

The results presented here were limited to immiscible flows to focus on capillary trapping. However, the PPU-C formulation has a straightforward extension to compositional simulation, and GEOS results with capillary trapping and dissolution trapping will be presented in a forthcoming publication.

Appendix A. Analytical steady-state solution for the 1D example

Here, we explain the procedure used to construct an analytical steady-state solution for the 1D example without hysteresis. At steady state, neither phase is flowing, so the net flux of each phase vanishes and the phase pressures become hydrostatic. Consequently, the capillary pressure varies linearly with depth, following the gravity-capillary equilibrium

$$P_c(z) = P_c^{\text{int}} - \Delta\rho\, g\,(z - z_{\text{int}}), \tag{A.1}$$

where $\Delta\rho = \rho_\ell - \rho_v > 0$ is the density difference, z is positive downward, z_{int} is the interface depth, and P_c^{int} is the interfacial capillary pressure. Since the CO_2 plume migrates to the top and accumulates beneath the higher-entry-pressure top layer, the steady state corresponds to the trapping configuration in which the interface capillary pressure equals the entry pressure of the top region, $P_c^{\text{int}} = p_e^{(\alpha)}$, and no more CO_2 is able to cross into the top layer. The resulting CO_2 bank extends below the interface down to the depth where the capillary pressure drops to the entry pressure of the bottom region, so that the bank thickness becomes

$$h = \frac{p_e^{(\alpha)} - p_e^{(\beta)}}{\Delta\rho\, g}, \tag{A.2}$$

Within the bank, we obtain the non-wetting phase saturation by inverting the (smoothed) capillary pressure curve of the bottom region. Consistent with the extended definition (5) used throughout this work, we first recover the underlying Brooks-Corey capillary pressure from the error-function mapping,

$$\widehat{P}_c^{(\beta)}(z) = \frac{2\, p_{\text{c,max}}^{(\beta)}}{\sqrt{\pi}}\, \text{erf}^{-1}\left(\frac{P_c(z)}{p_{\text{c,max}}^{(\beta)}}\right), \tag{A.3}$$

and then invert the Brooks-Corey equation to obtain the effective, and hence the non-wetting phase, saturation,

$$S_{nw}(z) = 1 - S_{\ell,c}^{(\beta)} - \left(1 - S_{\ell,c}^{(\beta)} - S_{v,r}^{(\beta)}\right)\left(\frac{\widehat{P}_c^{(\beta)}(z)}{p_e^{(\beta)}}\right)^{-\theta^{(\beta)}}, \qquad z \in [z_{\text{int}},\, z_{\text{int}} + h], \tag{A.4}$$

with $P_c(z)$ given by (A.1) using $P_c^{\text{int}} = p_e^{(\alpha)}$.

Moreover, the same construction applies to the top region as well. Because only a limited amount of the initial volume gets trapped in the capillary bank below the interface before it reaches capacity, the rest migrates to the top and accumulates beneath the no-flow boundary, forming another bank that contains the drained amount. So at steady state, there are two disconnected bodies of CO_2 plume in each region: one that is described earlier below the interface, and another one in the top extending over $z \in [0, z_c]$ in which

$$P_c(z) = p_e^{(\alpha)} + \Delta\rho\, g\, (z_c - z), \tag{A.5}$$

with the corresponding saturations again given by (A.3)–(A.4) using parameters of region α this time. Finally, the single unknown z_c can be estimated from conservation of the plume's total initial volume.

References

Aghili, J., Brenner, K., Hennicker, J., Masson, R., and Trenty, L. (2019). Two-phase discrete fracture matrix models with linear and nonlinear transmission conditions. *GEM-International Journal on Geomathematics*, 10(1):1.

Ahmed, R., Xie, Y., and Edwards, M. G. (2018). A cell-centred CVD-MPFA finite volume method for two-phase fluid flow problems with capillary heterogeneity and discontinuity. *Transport in Porous Media*, pages 1–18.

Alali, A. H., Hamon, F. P., Mallison, B. T., and Tchelepi, H. A. (2021). Finite-volume simulation of capillary-dominated flow in matrix-fracture systems using interface conditions. *Computational Geosciences*, 25(1):17–33.

Aziz, K. and Settari, A. (1979). *Petroleum reservoir simulation*, volume 476. Applied Science Publishers London.

Bachu, S., Gunter, W., and Perkins, E. (1994). Aquifer disposal of co2: hydrodynamic and mineral trapping. *Energy Conversion and management*, 35(4):269–279.

Bassetto, S., Cancès, C., Enchéry, G., and Tran, Q.-H. (2022). On several numerical strategies to solve richards' equation in heterogeneous media with finite volumes. *Computational geosciences*, 26(5):1297–1322.

Benson, S., Cook, P., Anderson, J., Bachu, S., Nimir, H. B., Basu, B., Bradshaw, J., Deguchi, G., Gale, J., von Goerne, G., Heidug, W., Holloway, S., Kamal, R., Keith, D., Lloyd, P., Rocha, P., Senior, B., Thomson, J., Torp, T., Wildenborg, T., Wilson, M., Zarlenga, F., and Zhou, D. (2005). Underground geological storage. In Metz, B., Davidson, O., de Coninck, H., Loos, M., and Meyer, L., editors, *IPCC Special Report on Carbon Dioxide Capture and Storage*, chapter 5, pages 195–276. Cambridge University Press, Cambridge, UK and New York, NY, USA.

Bosma, S. B. M. (2021). *Algorithms and Discretization Schemes for Efficient Simulation of Multiphase Flow and Transport in Porous Media*. Ph.D. dissertation, Stanford University, Stanford, CA. Department of Energy Resources Engineering. Advisor: Hamdi Tchelepi.

Brenier, Y. and Jaffré, J. (1991). Upstream differencing for multiphase flow in reservoir simulation. *SIAM Journal on Numerical Analysis*, 28(3):685–696.

Brenner, K., Cancès, C., and Hilhorst, D. (2013). Finite volume approximation for an immiscible two-phase flow in porous media with discontinuous capillary pressure. *Computational Geosciences*, 17(3):573–597.

Brenner, K., Groza, M., Jeannin, L., Masson, R., and Pellerin, J. (2017). Immiscible two-phase Darcy flow model accounting for vanishing and discontinuous capillary pressures: application to the flow in fractured porous media. *Computational Geosciences*, 21(5-6):1075–1094.

Brenner, K., Hennicker, J., Masson, R., and Samier, P. (2018). Hybrid-dimensional modelling of two-phase flow through fractured porous media with enhanced matrix fracture transmission conditions. *Journal of Computational Physics*, 357:100–124.

Brenner, K., Masson, R., Quenjel, E.-H., and Droniou, J. (2022). Total velocity-based finite volume discretization of two-phase darcy flow in highly heterogeneous media with discontinuous capillary pressure. *IMA Journal of Numerical Analysis*, 42(2):1231–1272.

Brooks, R. and Corey, T. (1964). Hydraulic properties of porous media. *Hydrology Papers, Colorado State University*.

Bruant, R., Guswa, A., Celia, M., and Peters, C. (2002). Safe storage of co2 in deep saline aquifers. *Environmental Science & Technology*, 36(11):240A–245A.

Bui, Q. M., Hamon, F. P., Castelletto, N., Osei-Kuffuor, D., Settgast, R. R., and White, J. A. (2021). Multigrid reduction preconditioning framework for coupled processes in porous and fractured media. *Computer Methods in Applied Mechanics and Engineering*, 387:114111.

Burdine, N. (1953). Relative permeability calculations from pore size distribution data. *Journal of Petroleum Technology*, 5(03):71–78.

Cancès, C. (2009). Finite-volume scheme for two-phase flows in heterogeneous porous media involving capillary pressure discontinuities. *ESAIM: Mathematical Modelling and Numerical Analysis*, 43(5):973–1001.

Carlson, F. M. (1981). Simulation of relative permeability hysteresis to the nonwetting phase. In *SPE Annual Technical Conference and Exhibition*. Society of Petroleum Engineers.

Chehade, P., Ramsay, T., Raguenel, M., Gacem, M., Ronot, C., Kloucha, C., Jellema, R., Hamon, F., Gross, H., Bourgeois, F., et al. (2024). Assessment of co2 storage capacities and identification of operational risks using large basin-scale multi-physics simulation on unstructured mesh. In *Abu Dhabi International Petroleum Exhibition and Conference*, page D031S083R006. SPE.

Corey, A. T. (1954). The interrelation between gas and oil relative permeabilities. *Producers monthly*, 19(1):38–41.

Enchéry, G., Eymard, R., and Michel, A. (2006). Numerical approximation of a two-phase flow problem in a porous medium with discontinuous capillary forces. *SIAM Journal on Numerical Analysis*, 43(6):2402–2422.

Ennis-King, J. and Paterson, L. (2002). Engineering aspects of geological sequestration of carbon dioxide. In *SPE Asia Pacific Oil and Gas Conference and Exhibition*, pages SPE–77809. SPE.

Evje, S. and Friis, H. A. (2012). Numerical treatment of two-phase flow in capillary heterogeneous porous media by finite-volume approximations. *International Journal of Numerical Analysis & Modeling*, 9(3).

Flett, M., Gurton, R., and Taggart, I. (2004). The function of gas-water relative permeability hysteresis in the sequestration of carbon dioxide in saline formations. In *SPE Asia pacific oil and gas conference and exhibition*, pages SPE–88485. SPE.

Gluyas, J. G. and Swarbrick, R. E. (2021). *Petroleum Geoscience*. Wiley-Blackwell, 2nd edition.

Hamon, F. P., Mallison, B. T., and Tchelepi, H. A. (2016). Implicit hybrid upwind scheme for coupled multiphase flow and transport with buoyancy. *Computer Methods in Applied Mechanics and Engineering*, 311:599–624.

Hamon, F. P., Mallison, B. T., and Tchelepi, H. A. (2018). Implicit hybrid upwinding for two-phase flow in heterogeneous porous media with buoyancy and capillarity. *Computer Methods in Applied Mechanics and Engineering*, 331:701–727.

IPCC (2022). Climate change 2022: Mitigation of climate change. contribution of working group iii to the sixth assessment report.

Kachuma, D., Hasanzade, R., Tomin, P., Thomadakis, M. E., Franc, J., Magri, V. A., Byer, T. J., Cusini, M., Settgast, R. R., Gross, H., et al. (2026). High-resolution simulations of geological co2 injection: Application to the spe11 benchmark. *SPE Journal*, 31(01):680–696.

Killough, J. E. (1976). Reservoir simulation with history-dependent saturation functions. *SPE Journal*, 16(1):37–48.

Kovscek, A. R., Nordbotten, J. M., and Fernø, M. (2024). Scaling up fluidflower results for carbon dioxide storage in geological media. *Transport in Porous Media*, 151(5):975–1002.

Krevor, S., Blunt, M. J., Benson, S. M., Pentland, C. H., Reynolds, C., Al-Menhali, A., and Niu, B. (2015). Capillary trapping for geologic carbon dioxide storage–from pore scale physics to field scale implications. *International Journal of Greenhouse Gas Control*, 40:221–237.

Land, C. (1968). Calculation of imbibition relative permeability for two-and three-phase flow from rock properties. *Old SPE Journal*, 8(2):149–156.

Larsen, J. and Skauge, A. (1998). Methodology for numerical simulation with cycle-dependent relative permeabilities. *SPE Journal*, 3(02):163–173.

Lenormand, R., Zarcone, C., and Sarr, A. (1983). Mechanisms of the displacement of one fluid by another in a network of capillary ducts. *Journal of Fluid Mechanics*, 135:337–353.

Leverett, M. (1941). Capillary behavior in porous solids. *Transactions of the AIME*, 142(1):152–169.

Metz, B., Davidson, O., De Coninck, H. C., Loos, M., and Meyer, L. (2005). *IPCC Special Report on Carbon Dioxide Capture and Storage*. Cambridge University Press, Cambridge, UK, 1st edition.

Ni, H., Li, B., Darraj, N., Ren, B., Harris, C., Krishnamurthy, P. G., Bukar, I., Berg, S., Snippe, J., Ringrose, P., et al. (2025). The impact of capillary heterogeneity on co2 flow and trapping across scales. *Earth-Science Reviews*, page 105257.

Niessner, J., Helmig, R., Jakobs, H., and Roberts, J. E. (2005). Interface condition and linearization schemes in the Newton iterations for two-phase flow in heterogeneous porous media. *Advances in Water Resources*, 28(7):671–687.

Nordbotten, J. M. and Celia, M. A. (2011). *Geological storage of CO2: modeling approaches for large-scale simulation*. John Wiley & Sons.

Nordbotten, J. M., Ferno, M. A., Flemisch, B., Kovscek, A. R., and Lie, K.-A. (2024). The 11th society of petroleum engineers comparative solution project: Problem definition. *SPE Journal*, 29(05):2507–2524.

Nordbotten, J. M., Fernø, M. A., Flemisch, B., Kovscek, A. R., Lie, K.-A., Both, J. W., Møyner, O., Sandve, T. H., Ahusborde, E., Bauer, S., Chen, Z., Class, H., Di, C., Ding, D., Element, D., Firoozabadi, A., Flauraud, E., Franc, J., Gasanzade, F., Ghomian, Y., Giddins, M. A., Green, C., Fernandes, B. R. B., Hadjisotiriou, G., Hammond, G., Huang, H., Kachuma, D., Kern, M., Koch, T., Krishnamurthy, P., Lye, K. O., Landa-Marbán, D., Nole, M., Orsini, P., Ruby, N., Salinas, P., Sayyafzadeh, M., Solovský, J., Torben, J., Turner, A., Voskov, D. V., Wendel, K., and Youssef, A. A. (2025). Benchmarking CO_2 storage simulations: Results from the 11th Society of Petroleum Engineers comparative solution project. *International Journal of Greenhouse Gas Control*, 148:104519.

Orr Jr, F. M. (2004). Storage of carbon dioxide in geologic formations. *Journal of Petroleum Technology*, 56(09):90–97.

Papafotiou, A., Sheta, H., and Helmig, R. (2010). Numerical modeling of two-phase hysteresis combined with an interface condition for heterogeneous porous media. *Computational Geosciences*, 14(2):273–287.

Pruess, K., Xu, T., Apps, J., and Garcia, J. (2003). Numerical modeling of aquifer disposal of co2. *SPE Journal*, 8(1):49–60.

Riaz, A., Hesse, M., Tchelepi, H., and Orr, F. (2006). Onset of convection in a gravitationally unstable diffusive boundary layer in porous media. *Journal of Fluid Mechanics*, 548:87–111.

Saadatpoor, E., Bryant, S. L., and Sepehrnoori, K. (2010). New trapping mechanism in carbon sequestration. *Transport in porous media*, 82(1):3–17.

Sammon, P. H. (1988). An analysis of upstream differencing. *SPE Reservoir Engineering*, 3(3):1053–1056.

Settgast, R. R., Aronson, R. M., Besset, J. R., and et al. (2024). Geos: A performance portable multi-physics simulation framework for subsurface applications. *Journal of Open Source Software*, 9(102):6973.

Spiteri, E. J. and Juanes, R. (2006). Impact of relative permeability hysteresis on the numerical simulation of wag injection. *Journal of Petroleum Science and Engineering*, 50(2):115–139.

Townsend, A., Raji, N., and Zapantis, A. (2020). The value of carbon capture and storage (ccs). Global CCS Institute.

Van Duijn, C. J., Molenaar, J., and De Neef, M. J. (1995). The effect of capillary forces on immiscible two-phase flow in heterogeneous porous media. *Transport in Porous Media*, 21(1):71–93.

Zhang, Q., Geiger, S., Storms, J. E., Voskov, D. V., Jackson, M. D., Hampson, G. J., Jacquemyn, C., and Martinius, A. W. (2025). Capillary pinning in sedimentary rocks for co2 storage: Mechanisms, terminology and state-of-the-art. *International journal of greenhouse gas control*, 144:104385.